

CHANGES: THE PAST, PRESENT, AND FUTURE OF THE NEARBY DWARF GALAXY NGC 55^{1 2}

T. J. DAVIDGE

Dominion Astrophysical Observatory,
National Research Council of Canada, 5071 West Saanich Road,
Victoria, BC Canada V9E 2E7
tim.davidge@nrc.ca

Draft version April 8, 2024

ABSTRACT

Spectra that cover wavelengths from 0.6 to 1.1 μm are used to examine the behavior of emission and absorption features in a contiguous 22×300 arcsec region centered on the nearby dwarf galaxy NGC 55. This area includes the two largest star-forming complexes in the galaxy, as well as other star-forming structures in the little-explored north west part of the disk. Based on the relative strengths of various emission features measured over spatial scales of many tens of parsecs, it is concluded that the ionization states and sulphur abundances in most of the star-forming regions near the center of NGC 55 are similar. However, a large star-forming region is identified in the north west part of the disk at a projected distance of ~ 1 kpc from the galaxy center that has distinct ionization properties. In addition to tracing areas of present-day star formation, the spectra are also used to identify fossil star-forming regions by mapping the depth of the near-infrared Ca triplet. One such area is identified near the intersection of the major and minor axes. There is a corresponding concentration of bright red stars in archival [3.6] and [4.5] images that are part of a mass concentration that is structurally distinct from the surrounding disk. It is suggested that the area near the intersection of the major and minor axes in NGC 55 is a proto-nucleus. The spectra of bright unresolved sources that are blended stellar asterisms, compact HII regions, and star clusters are also discussed. The spectra of some of the HII regions contain Ca triplet absorption lines, signalling a concentration of stars in the resolution element that span many Myr. Six of the unresolved sources have spectroscopic characteristics that are indicative of C stars embedded in intermediate age clusters, and these are likely compact star clusters that are analogous to those in the Large Magellanic Cloud. The peculiar properties of NGC 55 have been well documented in the literature, and it is argued that these may indicate that NGC 55 is transforming into a dwarf lenticular galaxy.

Subject headings: galaxies:individual (NGC 55) – galaxies:ISM – galaxies:stellar content

1. INTRODUCTION

Studies of nearby galaxies lay the foundation for understanding the evolution of more distant systems. Given the wide diversity of galaxy types throughout the Universe, it is then important to examine the evolution of as many nearby galaxies as possible. At a distance of ~ 2.3 Mpc (Kudritzki et al. 2016 and references therein), NGC 55 is one of the nearest galaxies that is not a member of the Local Group. However, many of its properties remain uncertain, in large part because it is viewed with an almost edge-on orientation.

While NGC 55 has been classified as a Magellanic Irregular (de Vaucouleurs et al. 1991), the distribution of light at red and near-infrared wavelengths has a lenticular shape, and so differs from that of the edge-on Magellanic galaxy NGC 4236, which has a similar luminosity

and distance (Davidge 2018b). The disk of NGC 55 is lop-sided, with what appears to be a tidal arm extending in the general direction of its nearest large companion – NGC 300. Isolated HI clouds are found along the disk plane at projected distances of ~ 30 kpc from the main body of the galaxy (Westmeier et al. 2013). The HI disk of NGC 55 also shows signs of being disturbed, hinting at a chaotic past (Westmeier et al. 2013).

Despite having features that might be associated with tidal interactions, NGC 55 is not in a dense environment. NGC 55 and NGC 300 are the dominant members of a sub-system that is on the near side of the so-called Sculptor Group. The dwarf galaxies ESO294-010 and ESO410-005 are other possible members of this sub-group, which has an estimated crossing time that exceeds the Hubble time (Karachentsev et al. 2003). Other members of the so-called Sculptor Group are at larger distances from NGC 55 than might be inferred simply from their projected location on the sky.

Source confusion that is exacerbated by the orientation of NGC 55 on the sky makes it challenging to resolve individual stars except in the outer areas of the stellar disk and in the extraplanar regions. Still, NGC 55 was one of the first galaxies outside of the Local Group for which the detection of individual stars was claimed (Graham 1982). NGC 55 was also an early target of narrow-band photometric surveys to identify C stars (Pritchett et

¹ Based on observations obtained at the Gemini Observatory, which is operated by the Association of Universities for Research in Astronomy, Inc., under a cooperative agreement with the NSF on behalf of the Gemini partnership: the National Science Foundation (United States), the National Research Council (Canada), CONICYT (Chile), Ministério da Ciência, Tecnologia e Inovação (Brazil) and Ministerio de Ciencia, Tecnología e Innovación Productiva (Argentina).

² This research has made use of the NASA/IPAC Infrared Science Archive, which is operated by the Jet Propulsion Laboratory, California Institute of Technology, under contract with the National Aeronautics and Space Administration.

al. 1987). The C star frequency deduced from those data is significantly higher than in the LMC and SMC (Battinelli & Demers 2005), suggesting levels of star-forming activity in NGC 55 during intermediate epochs that exceed those in the LMC and SMC. Davidge (2018a) examined the spectroscopic properties of the northern half of the NGC 55 minor axis, and found that the Ca triplet lines near the disk plane have depths that are consistent with $[\text{Fe}/\text{H}] = -0.35$ and a luminosity-weighted age of 1 – 2 Gyr. A large C star frequency might then be expected.

Magrini, Goncalves, & Vajgel (2017) measure oxygen abundances in HII regions along the NGC 55 disk plane that are intermediate between those of the LMC and SMC (e.g. Carlos Reyes et al. 2015). The analysis of the spectra of bright supergiants in NGC 55 reveals LMC-like abundances (Castro et al. 2012; Kudritzki et al. 2016; Patrick et al. 2017). While there appears not to be a radial abundance gradient in the LMC (e.g. Toribio San Cipriano et al. 2017; Pagel et al. 1978), there is conflicting evidence about radial abundance trends in NGC 55. Kudritzki et al. (2016) find evidence for a metallicity gradient in the interstellar medium (ISM), while Magrini et al. (2017) find a flat radial abundance profile. Kudritzki et al. (2016) conclude that NGC 55 is accreting large amounts of gas. If this is the case then the chemical content of HII regions may not mirror that of older stars in the same part of the galaxy.

While HII regions are found throughout NGC 55, much of the present-day star-forming activity is concentrated in two star-forming complexes in the central kpc of the galaxy that have 30 Dor-like luminosities (Ferguson et al. 1996). Otte & Dettmar (1999) label these as H2 and H4 in their Figure 2. Recent star formation in these – and other – complexes has undoubtedly helped to shape the present-day spatial distribution of the ISM in NGC 55, including the excitation of a diffuse interstellar component that is found over much of the galaxy (e.g. Graham & Lawrie 1982; Hoopes et al. 1996; Ferguson et al. 1996; Otte & Dettmar 1999).

A substantial extraplanar ISM is present in NGC 55, and the properties of this gas provides additional insights into the evolution of the galaxy. The HI distribution of NGC 55 is not symmetric about the major axis (Westmeier et al. 2013), and the presence of bubbles, shells, and chimney structures in the ISM indicate that material is being heated and expelled from the disk. HII regions are found well off of the disk plane (Tullmann et al. 2003; Kudritzki et al. 2016), and Tullmann et al. (2003) measure metallicities that are lower than in the disk. Such low metallicities indicate that mechanisms other than the ejection of gas from the disk contribute to the extraplanar gas and dust. A population of HI clouds have been found around NGC 55 (Westmeier et al. 2013), and these might serve as a reservoir for fueling extraplanar star formation.

Davidge (2005) used deep GMOS images to probe the stellar content off of the disk plane, and found that the extraplanar environment is dominated by old stars. While finding old stars in this part of NGC 55 is not unexpected, the color of the extraplanar RGB is consistent with $[\text{M}/\text{H}] \sim -1.2$ to -1.3 . This is similar to the metallicity found in extraplanar HII regions, hinting at a flat age-metallicity relation in this part of the

galaxy. Tikhonov et al. (2005) estimate a similar metallicity from deep HST images of the same area.

It is apparent that NGC 55 has characteristics that may not be typical of Magellanic Irregular galaxies. In the present paper we discuss a grid of long-slit spectra of NGC 55 recorded with the Gemini Multi-Object Spectrograph (GMOS) on Gemini South (GS). A contiguous 0.4×5 arcmin area was observed, centered near the intersection of the major and minor axes. The target area covers regions to the south east of the minor axis that have been the subject of many previous studies (see above), as well as the less-studied area to the north west of the minor axis.

The primary goal is to examine the luminosity-weighted properties of the central regions of the galaxy, which is an environment that is expected to be rich in information about its past evolution. Integral field observations of this nature are a powerful means of investigating stellar content and galactic structure in complicated environments (e.g. Roth et al. 2018). The scientific benefits of integral field observations has motivated the development of instruments such as MUSE (e.g. Bacon et al. 2010), as well as software packages such as TYPHOON (Sturch & Madore 2012).

Spectra of compact sources with a FWHM that is comparable to that of the seeing disk, and so are unresolved, are also examined. With an image scale of 1 arcsec ~ 10 parsecs, then the majority of these sources are almost certainly blended asterisms, star clusters, or compact HII regions. The GMOS spectra are supplemented with archival GALEX (Martin et al. 2005), 2MASS (Skrutskie et al. 2006), and SPITZER (Werner et al. 2004) images. The GALEX images trace star formation over the past few tenths of a Gyr, while the 2MASS and SPITZER images trace stars that formed over a much longer time span and are the dominant contributor to overall stellar mass.

Details of the observations and the steps used to remove instrumental and atmospheric signatures are reviewed in Section 2. The GALEX, 2MASS, and Spitzer observations are discussed in Section 3, while the projected distribution of emission and absorption lines in the area surveyed with GMOS, including the spectroscopic properties of the largest star-forming complexes, are the subject of Section 4. The nature of unresolved sources are examined in Section 5. The paper closes in Section 6 with a discussion and summary of the results.

2. OBSERVATIONS & REDUCTIONS

2.1. Description of the Observations

The spectra discussed in this paper were recorded with GMOS (Hook et al. 2004) on GS for program GS-2017A-Q-98 (PI: Davidge). The GMOS detector is a mosaic of three 2048×4176 Hamamatsu CCDs. With on-sky sampling of 0.080 arcsec pixel $^{-1}$, the rectangular detector mosaic allows spectra to be recorded at wavelengths that are dispersed out of the 5.5×5.5 arcmin sky footprint. The detector was binned 4×4 pixels during read-out given the image quality and spectral resolution.

Individual spectra were recorded through a 5.5 arcmin long and 2 arcsec wide slit. The light was dispersed with the R400 grating (400 l/mm; $\lambda_{\text{blaze}} = 7640 \text{ \AA}$, $\lambda/\Delta\lambda \sim 500$ with a 2 arcsec slit). The grating was ro-

TABLE 1
DATES OF OBSERVATION

Pointing	Date Observed (UT 2017)
p10	July 13
p8	July 11
p6	July 10
p4	July 10
p2	July 3
Center	July 3
n2	July 13
n4	July 13
n6	July 13
n8	July 13
n10	July 24
n12	July 24
Minor Axis	July 3 + July 24

tated so that spectra were recorded with wavelengths at the detector center of either 8200 or 8500Å. Recording spectra with two central wavelengths allows holes in wavelength coverage due to gaps between CCDs to be filled during processing. An OG515 filter was deployed to suppress light from higher orders.

Thirteen contiguous pointings were observed that map the brightest central parts of NGC 55. Twelve of the pointings run parallel to the major axis, and these are referred to as the ‘disk’ pointings. The disk pointings sample the galaxy in 2 arcsec increments perpendicular to the major axis of NGC 55. The disk pointings together cover a 0.4×5 arcmin² area. The area observed is shown in Figure 1 against the backdrop of a SPITZER [3.6] image. The central co-ordinates and the dates of observation for each pointing are listed in Table 1. The naming convention in this table and for the remainder of the paper is such that ‘p’ and ‘n’ refer to positive and negative offsets perpendicular to the major axis. The number following ‘p’ or ‘n’ is the offset in arcsec from the major axis. The Center field runs along the major axis of the galaxy. Four 450 sec exposures were recorded at each disk pointing, with two exposures at each central wavelength.

Observations were also recorded with the slit placed along the minor axis. NGC 55 is viewed almost edge-on, and has a moderately compact light distribution perpendicular to the disk plane. Minor axis spectra were recorded with the galaxy stepped between two locations on the slit, so that the sky could be removed by subtracting successive spectra recorded at different step locations. Minor axis spectra were recorded on two nights, and eight 450 sec exposures were recorded in total. Negligible sky residuals in the processed minor axis spectrum at wavelengths where strong emission lines dominate the night sky signal are testament to the stability of the sky level when these data were recorded. The minor axis spectrum was discussed previously by Davidge (2018a).

The disk pointing spectra were not stepped along the slit, as the major axis of NGC 55 has a length that exceeds the GMOS slit length. While background sky is not sampled, the sky level for each pointing can still be estimated by comparing the signal from the sky-subtracted minor axis spectrum with the sky+galaxy spectrum at the point where the minor axis and disk spectra intersect (Section 2.3). An alternate observing strategy would be

to apply large angular offsets immediately following individual disk observations and record spectra of pristine sky. However, this lowers efficiency, as only half of the exposures would then sample the science target. Additional time is also required to offset and re-acquire the science field.

Calibration exposures that are required to remove instrumental and atmospheric signatures from the spectra were also recorded. Calibrations that did not require time on-sky include: (1) bias frames that are recorded on a daily basis by Gemini staff; (2) images of dispersed light from a continuum source in the facility calibration unit (GCAL) that were recorded midway through observing sequences; and (3) spectra of a CuAr arc that is also in GCAL, recorded at the end and/or beginning of nights. The arcs were recorded with the same central wavelengths as the science spectra. On-sky calibrations consisted of (1) spectra of the dO star Feige 110 to gauge contamination from telluric absorption features and wavelength response, and (2) dispersed light of the twilight sky that are used to construct a ‘twilight’ flat field frame. The twilight flat is used to correct for differences in slit illumination between sources on the sky and the flat-field lamp in GCAL (Section 2.2).

Neither the NGC 55 disk nor Feige 110 spectra were recorded during photometric conditions. Hence, absolute fluxes can not be determined from the NGC 55 spectra. Still, as the NGC 55 spectra are contiguous and all intersect the minor axis spectrum then they can be calibrated in a self-consistent internal manner, such that the shape (but not the zeropoint) of the spectral energy distribution is retained.

2.2. Initial Processing: Removal of Instrumental Signatures

All processing was done using routines in the IRAF¹ data reduction package. The initial processing removed static instrument signatures that originate in the optics and detector. To start, a median bias frame was constructed for each night that data were recorded, and the result was subtracted from all exposures obtained on that night. The GMOS CCDs are read out with

¹ IRAF is distributed by the National Optical Astronomy Observatories, which are operated by the Association of Universities for Research in Astronomy, Inc., under cooperative agreement with the National Science Foundation.

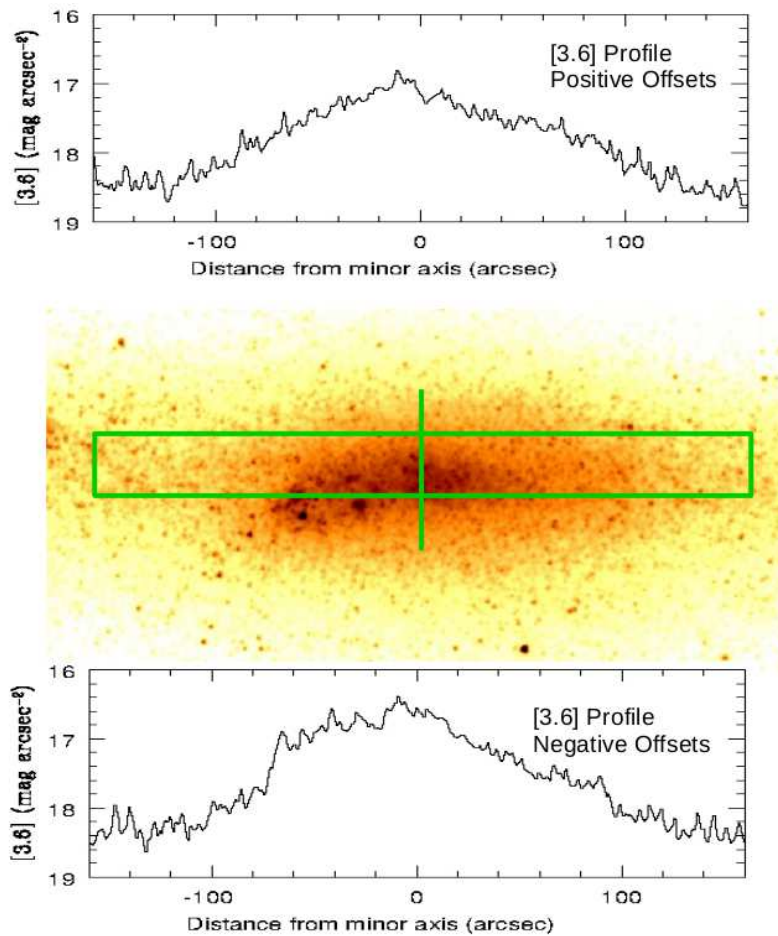


FIG. 1.— (Middle panel) [3.6] image of NGC 55, showing the area observed with GMOS. The image was recorded for the program described by Sheth et al. (2010), and was downloaded in processed form from the NASA Extragalactic Database. The image has been rotated so that the NGC 55 disk plane lies along the horizontal axis. North is towards the upper right hand corner, and East is towards the upper left hand corner. The green box has a length of 5 arcmin and a width of 0.4 arcmin, and shows the area covered by the disk pointings. The vertical green line marks the slit location for the minor axis pointing. (Upper and lower panels) Mean [3.6] light profiles of the regions that have positive and negative offsets from the major axis. The differences between the two light profiles foreshadows the diversity of properties in the spectra. The light profile defined from positive offsets – where there is little or no contamination from the star-forming complexes H2 and H4 – follows an exponential on each side of the minor axis. The negative offset light profile is less well-defined and is not symmetric about the minor axis; aside from a bump to the left of the minor axis that is due to H2 and H4, the surface brightness near the the minor axis is a few tenths of a magnitude arcsec^{-2} higher than that extrapolated from the disk light profile at larger positive radii.

twelve amplifiers, and the bias-subtracted data were adjusted for amplifier-to-amplifier differences in gain. Bad pixels and columns were identified using existing maps of these devices. Cosmic-rays were found by identifying pixels that fell above the median value of surrounding pixels by a pre-defined threshold. The threshold was selected to prevent triggering on noise events and bright emission features in the science spectra. Bad pixels and cosmic rays were repaired by interpolating between ‘good’ pixels.

Flat-fielding was done in two steps. First, each spectrum was divided by flat-field frames that used the GCAL continuum lamp as the source of illumination. These flat-field frames have a high S/N ratio, and correct for pixel-to-pixel and CCD-to-CCD differences in quantum efficiency as well as for vignetting along the slit. However, the optical feed from GCAL does not follow the same light path as signal from the sky, and so the slit is illuminated by GCAL in a slightly different manner than the science data. This is remedied in the second flat-fielding step, in which the twilight sky

flat is used to compensate for differences between GCAL and sky illumination. Absorption features in the twilight flat, which is a dispersed spectrum of scattered sunlight, were suppressed by collapsing the twilight flat along the dispersion axis after division by the GCAL flat. This wavelength smoothing also increased the signal-to-noise ratio of the twilight flat. The result is an achromatic illumination correction that was applied to the science data.

The final step in the initial processing was to correct for geometric distortions introduced by the GMOS optics. These cause emission and absorption features that should be straight in the direction perpendicular to the dispersion axis to instead appear curved. A distortion map was constructed by tracing bright emission lines in a mean arc spectrum, and the result was used to define a two-dimensional warping function to correct for these distortions. This relation was then applied to the science data.

2.3. Final Processing: Construction of Spectra for Analysis

The goals of the second phase of the processing are to remove telluric emission and absorption features, and adjust for instrumental variations in throughput. The spectra are also wavelength calibrated. The end product are spectra that can be used to examine the spectroscopic characteristics of emission and absorption features throughout the central regions of NGC 55.

The subtraction of the sky from the minor axis data was achieved by differencing pairs of observations recorded with the same central wavelength, but at different locations along the slit. Since the sky level is measured at the same location on the slit as the science data (albeit at slightly different times) then systematics that arise due to detector fringing and flat-fielding are suppressed. The resulting differenced two-dimensional spectra contain positive and negative versions of the target spectrum. Common spatial intervals were extracted from the negative and positive components, and a co-added spectrum was produced for each wavelength setting by subtracting the negative spectrum from the positive spectrum. Each co-added spectrum was wavelength calibrated, and the results at each wavelength setting were averaged together. Holes in the wavelength coverage due to gaps between CCDs were filled using signal from the other wavelength setting.

Sky emission in the disk spectra was removed using the sky-subtracted minor axis spectrum as a reference. After adjusting for variations in sky transparency, the difference between the sky-subtracted minor axis spectrum and the disk spectrum at the point of intersection is the sky spectrum for that disk pointing. Sky subtraction was checked by generating a light profile from the sky-subtracted spectra near $0.85\mu\text{m}$, and comparing the results to that obtained from 2MASS J-band images (Section 3). Good agreement between the light profiles was found. The sky-subtracted disk spectra were then wavelength calibrated and combined, with wavelength intervals that lacked signal again filled with spectra taken at the other wavelength setting.

The NGC 55 spectra were divided by the spectrum of Feige 110, which had been processed in parallel with the NGC 55 data. Dividing by the Feige 110 spectrum suppresses telluric absorption features and wavelength-dependent throughput variations. The wavelength response of the NGC 55 spectra is also normalized to that of a dO star, thereby simplifying the identification of the continuum. $\text{H}\alpha$ absorption is present in the Feige 110 spectrum, and this was removed by fitting this part of the spectrum with a Vogt profile and then subtracting the fit. Lines of the Paschen series are not evident in the Feige 110 spectrum.

Two sets of spectra were constructed for NGC 55. For one set a low-order continuum function was fit to each ratioed NGC 55 spectrum, and the spectra were divided by the results. These continuum-normalized spectra are used to measure the equivalent widths of various lines, and are the basis for spectra displayed in figures throughout the paper. To generate the second set, the ratioed spectra were multiplied by a response function that recovered the spectral energy distribution (SED) of each offset spectrum, using the Feige 110 spectrum as a

reference. These spectra are used to determine relative line strengths.

3. GALEX, 2MASS, AND SPITZER OBSERVATIONS

Archival ground and space-based images that span a broad range of wavelengths provide supplemental information for understanding the evolution of NGC 55. Images of NGC 55 taken as part of surveys and science programs conducted with GALEX and SPITZER, as well as images recorded as part of the 2MASS survey, are considered here. The angular resolutions of the GALEX and SPITZER datasets are comparable to those of the GMOS spectra.

The SPITZER observations are [3.6] and [4.5] images discussed by Sheth et al. (2010). With the exception of luminous red supergiants (RSGs) and AGB stars that belong to young and moderately young populations, much of the light in [3.6] and [4.5] originates from older giant branch stars that trace stellar mass. Dust extinction is a concern for NGC 55 as it is a star-forming galaxy that is viewed almost edge-on, and absorption by dust along the line-of-sight is greatly reduced in [3.6] and [4.5] when compared with images in the visible and UV.

J and K s images of NGC 55 were taken from the 2MASS Large Galaxy Atlas (Jarrett et al. 2003). A significant contribution to the integrated light in these filters comes from older evolved red stars that trace the stellar mass of the galaxy. The 2MASS images have ~ 3 arcsec FWHM angular resolution with a shallow photometric depth, and so their use in the current study is restricted to broad-band color measurements near the center of the galaxy. Finally, FUV and NUV images from the GALEX Ultraviolet Atlas of Nearby Galaxies (Gil de Paz et al. 2007) are also examined. These highlight areas of recent star formation as well as pockets of high dust obscuration.

Processed images from all three datasets were downloaded from the NASA Extragalactic Database². These were rotated to place the major axis of NGC 55 along the horizontal axis, and then re-sampled to match the pixel scale of the SPITZER data. Sky levels were measured in areas that are free of light from NGC 55, and the results were subtracted from the images.

There are areas of extended emission in the [3.6] image in Figure 1, some of which correspond to concentrations of hot stars that are also visible in the GALEX images (see below). Individual unresolved luminous sources are also sprinkled across the [3.6] image. The intrinsic spatial resolution of the SPITZER data is coarse (~ 20 pc at the distance of NGC 55, based on 2 arcsec FWHM image quality measured in the [3.6] images), and so any apparent point sources likely contain signal from more than one star. This being said, highly evolved stars are intrinsically luminous objects with comparatively low effective temperatures, and so stand out in [3.6] and [4.5] with respect to the background light that originates predominantly from warmer objects. The contrast with respect to background light is further enhanced if the evolved stars are surrounded by hot circumstellar dust, as can occur around intermediate mass stars that are nearing the end of their evolution. In Section 5 it is shown that some unresolved sources in the Spitzer obser-

² <http://www.ned.ipac.caltech.edu>

vations have spectroscopic signatures that are indicative of highly evolved AGB stars.

Light profiles of the positive and negative disk pointings were constructed from the [3.6] observations by summing the light in each angular interval on either side of the major axis, and the results bracket the [3.6] image in Figure 1. In both cases the profile to the right of the minor axis defines a disk-like exponential, suggesting that single sources do not dominate the light profile in this part of the galaxy. However, the positive and negative profiles to the left of the minor axis are different. The areas of star formation in and around the sources H2 and H4 (Otte & Dettmar 1999) produce prominent peaks in the left hand side of the negative offset light profile. The light from H2 and H4 in [3.6] likely originates from a mix of luminous red stars, thermal emission, and – if there are stars present with ages ≤ 4 Myr – nebular continuum emission (e.g. Figure 12 of Byler et al. 2017).

There is also a modest structure in the negative offset profile that is centered on the minor axis. An extrapolation of the portion of the negative profile that is to the right of the minor axis to the center of the galaxy indicates that the area within $\pm 15 - 20$ arcsec of the minor axis has a surface brightness that is a few tenths of a magnitude arcsec^{-2} higher than what is expected for a purely exponential disk. There are pockets of relatively deep Ca triplet absorption in this part of the galaxy that are accompanied by luminous red stars in the [3.6] image (Section 4).

In contrast to the negative offset profile, the positive offset profile follows an exponential to the left of the minor axis, but flattens near the left hand edge of the panel due to light from the tail of stars and gas that emerges from this part of the galaxy. Similar behaviour at large radii to the left of the minor axis is seen at negative offsets. The distinct break in the light profiles indicates that the tail of stars and gas is structurally distinct from the main body of the disk, as might be expected if it is a tidal feature.

The diverse range of environments and populations sampled by GMOS becomes apparent when examining the broad-band colors generated from the images. FUV–NUV, J–K, and [3.6]–[4.5] were computed with the native angular resolution of each dataset (i.e. not balanced over the entire suite of images), and the results are shown in Figure 2. Areas with the bluest colors are shown in white, while darker shades correspond to progressively redder colors.

The mottled appearance of the FUV–NUV map in Figure 2 highlights the spatial distribution of hot, young stars and star-forming regions, coupled with non-uniformities in line-of-sight extinction. FUV–NUV colors indicate that areas of large-scale star formation occupy much of the area to the immediate left of the minor axis in the GMOS field, while smaller, more isolated star-forming regions are present to the right of the minor axis. The large-scale serpentine-like structure in the left hand half of the FUV–NUV map appears to track bubbles and areas of star formation triggered by outflowing material that has been identified in previous studies.

There is less variation in $J - K$ in the area to the right of the minor axis in Figure 2 than to the left of this axis. There is a gradient in $J - K$ moving away from the large star-forming complexes along both the major and

minor axes, in the sense of $J - K$ becoming smaller (lighter colors in Figure 2) with increasing distance. While there is nebular emission combined with non-uniform obscuration near the center of NGC 55, the overall trend in $J - K$ likely is due to systematic variations in stellar content. If such variations in stellar content are present then a gradient in the depth of the Ca triplet might be expected. In fact, Davidge (2018a) finds a gradient in the depth of the Ca triplet along the minor axis of NGC 55. This gradient was attributed to metallicity decreasing with increasing distance from the major axis, and the sense of the $J - K$ gradient is consistent with this. In summary, the $J - K$ and FUV–NUV color distributions in Figure 2 indicate that the areas to the right of the minor axis track more closely the disk mass profile of NGC 55 than those to the left of the minor axis, as they are less affected by areas of recent large-scale star formation.

When considered over angular scales of a few tens of arcsec or more, the [3.6]–[4.5] color is uniform across much of NGC 55, due to the muted sensitivity of the Rayleigh-Jeans tail of the SEDs to temperature variations, coupled with the lower sensitivity of integrated colors at these wavelengths to reddening. Still, there are spatially extended areas that have very red [3.6]–[4.5] colors that coincide with star-forming regions in the FUV–NUV map. The red [3.6]–[4.5] color in these regions is likely due to dust that has been heated by young, hot stars. There are also a number of discrete sources scattered across the [3.6]–[4.5] map. These are the same unresolved sources discussed earlier in this section, and these are more conspicuous in Figure 2 because the large-scale light variation due to the main body of the galaxy is suppressed when colors are displayed. The detection of these objects in the [3.6]–[4.5] map is consistent with them being highly evolved stars or clusters in which the light is dominated by luminous red stars.

4. THE PROJECTED DISTRIBUTION OF EMISSION AND ABSORPTION FEATURES

The images discussed in Section 3 indicate that the area examined with GMOS samples a broad mix of populations and environments. This is further demonstrated in Figure 3, where the mean spectra of three angular intervals along the major axis are compared. The areas over which the mean spectra were generated are marked in the bottom panel of Figure 2.

Area-to-area differences in emission line strengths are evident in the left hand panel of Figure 3, as might be expected from the color measurements discussed in Section 3. Emission lines are strongest in the spectrum of Area 1, which contains the H4 star-forming complex. The FUV–NUV and [3.6]–[4.5] color maps indicate that there is strong UV emission combined with significant amounts of dust emission in Area 1. Smaller – but nonetheless significant – area-to-area differences are also seen in the depths of the Ca triplet lines in the right hand panel of Figure 3. That the Ca triplet lines do not differ markedly in these spectra suggests that veiling by continuum emission may not be a major factor when interpreting NGC 55 spectra near 8600Å.

To trace spectroscopic characteristics, line indices were defined for key emission ($H\alpha + \text{NII}$; He I 6678; [SII]6717+6731; He I 7065; and [SIII]9069) and absorption (Ca3 and CN7900) features. These features were

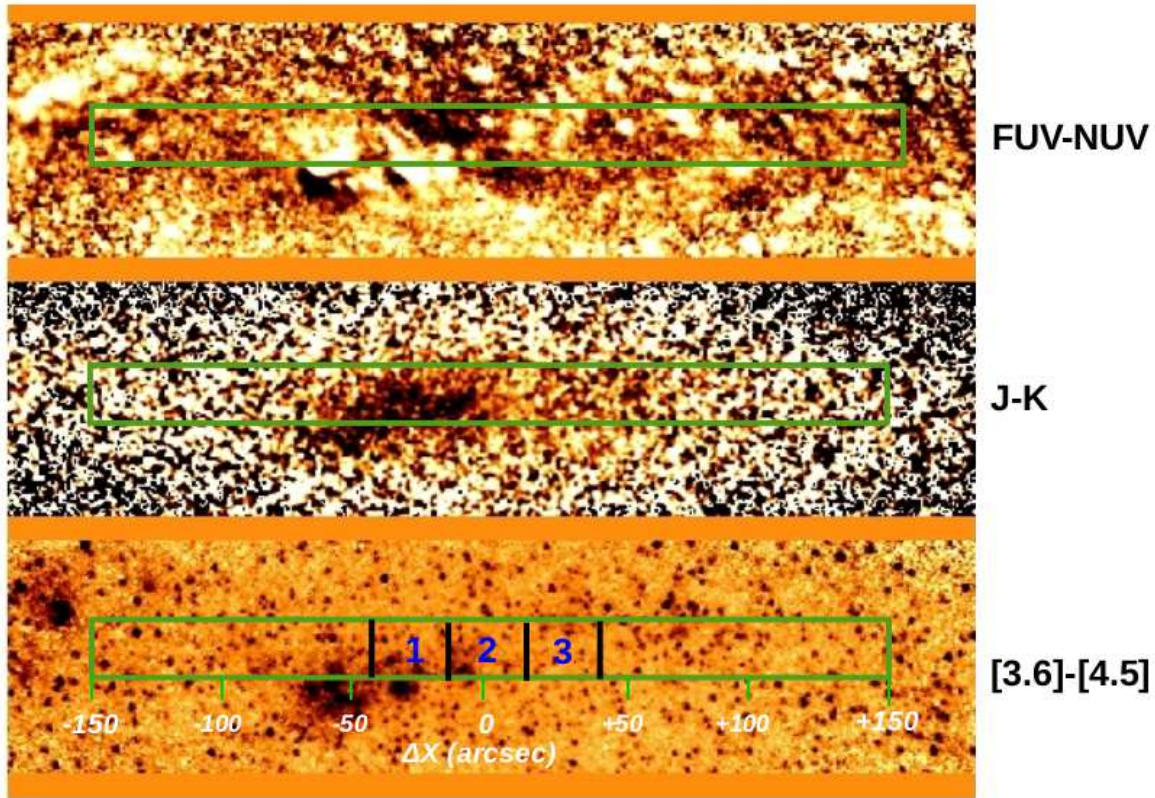


FIG. 2.— FUV-NUV (top panel), J-K (middle panel), and [3.6]-[4.5] (bottom panel) colors near the center of NGC 55. The green box in each panel marks the area observed with GMOS. Areas with the bluest colors are shown in white, while the darkest areas have the reddest colors. The three angular intervals used to construct the spectra shown in Figure 3 are marked in the bottom panel, along with offsets from the minor axis (ΔX). The complex distribution of the light near the center of NGC 55 is evident in the broad-band colors. Concentrated pockets of recent star-forming activity with blue FUV-NUV colors due to early-type stars, and red colors in $J - K$ and [3.6]-[4.5] due to thermal and continuum emission, are obvious to the left of the minor axis. The area to the right of the minor axis samples a part of the galaxy that has been less active in terms of recent star formation, although pockets of hot blue stars are still present, and these are seen in the GMOS spectra (Section 4).

selected based on their strengths and astrophysical significance. The index passbands are listed in Table 2, where wavelength intervals that sample the target line (or lines) as well as continuum measurements that straddle the line(s) are specified. All indices are measured as equivalent widths. The 2 arcsec slit width largely defines the angular resolution of these data, and so spectra were binned along the spatial direction prior to measuring indices so that each spaxial samples 2×2 arcsec.

4.1. Emission Lines

The spatial distribution of $H\alpha$ emission in the central regions of NGC 55 is examined in the top panels of Figures 4 - 6. The numbers in the $H\alpha$ panels are line strengths, normalized to that in $H2$. The line strengths were normalized to $H2$ because an absolute flux calibration was not possible (Section 2), and this is where $H\alpha$ is strongest. The line strengths were measured over 6×6 arcsec² areas to boost the signal to noise ratio near the slit edges, where the signal is lowest. The $H\alpha$ measurements are displayed with a logarithmic stretch.

The relative strengths of other emission features, normalized to $H\alpha$, are also shown in Figures 4 - 6. The line ratios are displayed with a linear stretch, and the numbers shown in these panels reflect signal averaged over 6×6 arcsec² areas. There is a tendency for the $H\alpha$ measurements and line ratios near the right hand

edge of Figure 6 to depart markedly from values that are more typical for the region observed with GMOS, and this is due to the low surface brightness near the slit edges (Figure 1).

$H\alpha$ is blended with [NII]6584 in these spectra. The contribution that [NII] makes to the combined $H\alpha$ + [NII] signal was estimated using the IRAF task SPLOT. The $H\alpha$ and [NII]6584 lines were both fit with two Gaussians having the same width, and the results indicate that [NII] contributes $\sim 6\%$ of the total signal in the central regions of NGC 55, with a $\pm 1\%$ dispersion. This is consistent with line strengths measured in NGC 55 HII regions by Magrini et al. (2017), where [NII] contributes $\sim 5\%$ on average to the combined $H\alpha$ and [NII]6584 flux, with a standard deviation of $\pm 3\%$. The measurements made by Webster & Smith (1983) have a mean [NII]/ $H\alpha$ = 0.06. Therefore, while [NII]6584 contributes to the $H\alpha$ measurements in Figures 4 - 6, it is at only at the few percent level.

Figure 1 of Graham & Lawrie (1982) shows the distribution of [OIII]5007 emission in part of the area observed with GMOS, and the distribution of [OIII] emission is similar to that defined by the $H\alpha$ index in Figures 4 and 5³. A feature that Graham & Lawrie identify as

³ Much of the area covered in Figure 6 falls outside of the area observed by Graham & Lawrie (1982).

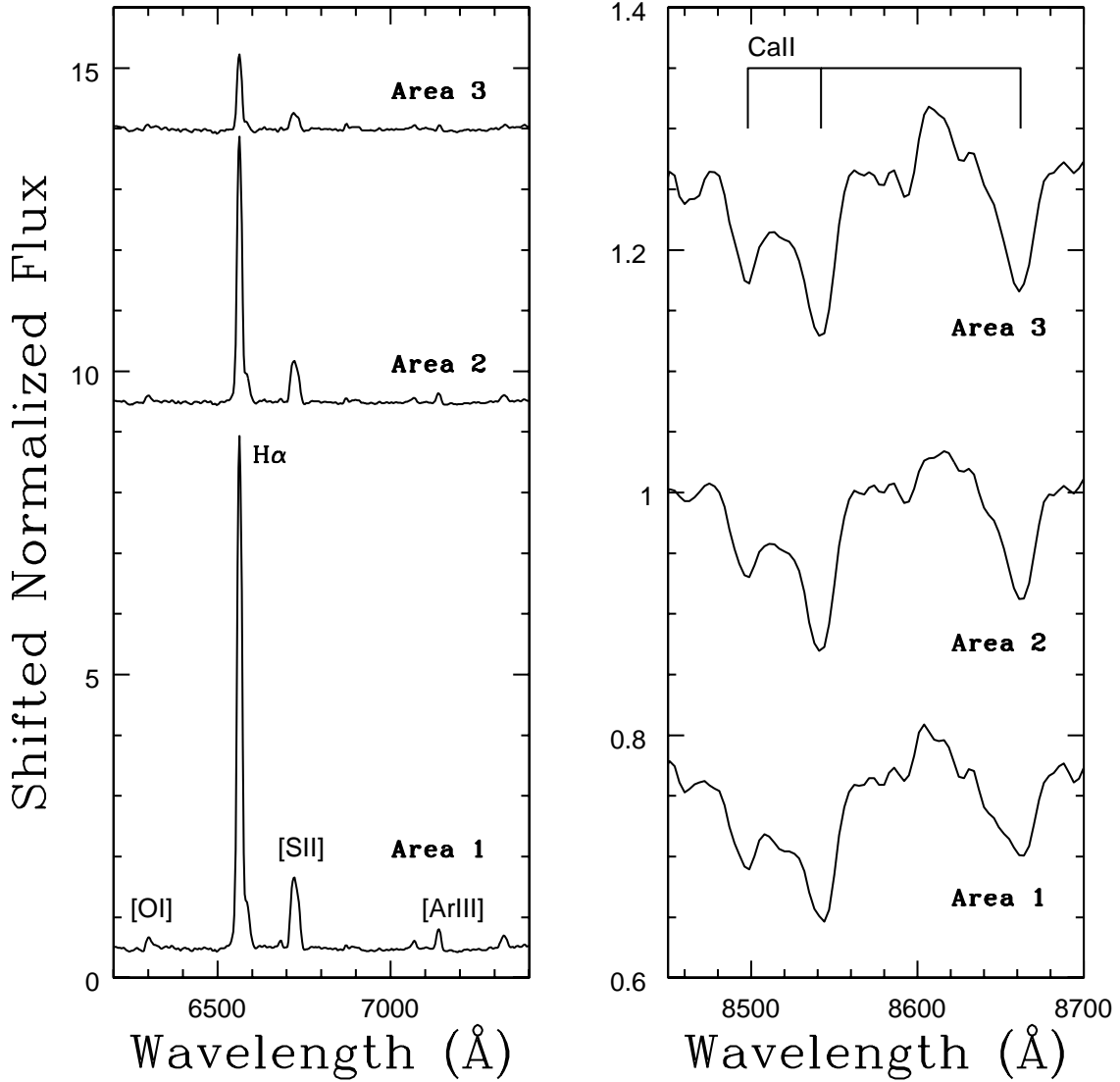


FIG. 3.— Mean spectra of the three angular intervals centered on the minor axis of NGC 55 that are marked in the lower panel of Figure 2. Wavelengths near $H\alpha$ and the Ca triplet are shown. The spectra have been normalized to the continuum, and shifted along the vertical axis for display purposes. There is a gradient in emission line strengths from Area 1 to Area 3. The strong emission lines in the Area 1 spectrum originate in the H4 star-forming complex. That the variations in the Ca lines are much more subtle than those among the emission lines suggests that veiling by continuum emission near 8600Å is modest.

TABLE 2
INDEX PASSBANDS

Index	Feature (Å)	Continuum 1 (Å)	Continuum 2 (Å)
$H\alpha$	6530–6610	6450–6530	6650–6690
[SII]6717+6731	6702–6749	6689–6702	6749–6762
HeI 7065	7044–7083	7005–7044	7083–7121
[SIII]9069	9040–9090	8938–9040	9090–9192
CN7900	7875–7975	7800–7875	7975–8050
Ca3	8480–8680	8450–8480	8680–8710

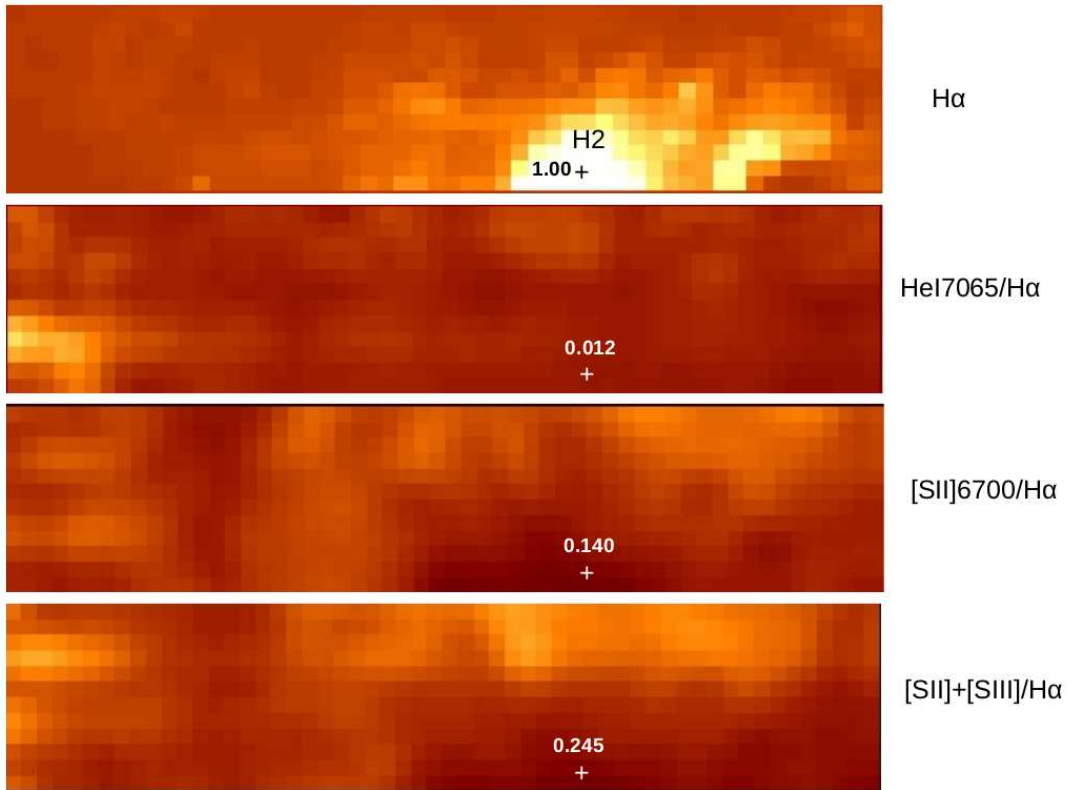


FIG. 4.— Spatial distribution of $H\alpha$ line strengths (top panel), and the relative strengths of three emission lines with respect to $H\alpha$ (lower three panels). The angular interval examined in this figure is the left hand third of the GMOS field shown in Figure 1. The numbers in the top panel show the relative strength of $H\alpha$ emission normalised to that of H2. The numbers in the other panels show relative line strengths with respect to $H\alpha$. $[SII]+[SIII]$ is the sum of the $[SII]$ 6717+6731 Å doublet and the $[SIII]$ 9069 line strengths. $H\alpha$ measurements are displayed with a logarithmic stretch while line ratios are shown with a linear stretch. The star-forming complex identified as H2 in Figure 2 of Otte & Dettmar (1999) is marked.

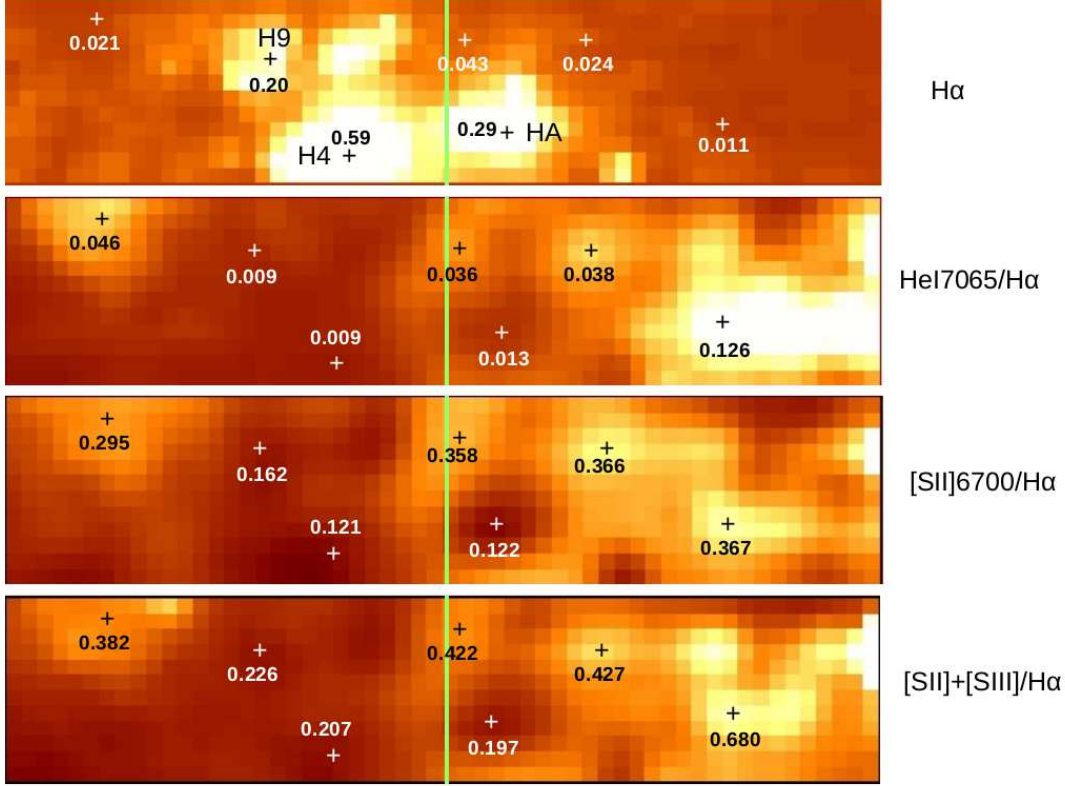


FIG. 5.— Same as Figure 4, but for the middle third of the area observed with GMOS. The surface brightness at visible/red wavelengths is highest in this area. The minor axis of NGC 55 is indicated by the green line. The star-forming complex H4 (Figure 2 of Otte & Dettmar 1999) dominates the $H\alpha$ distribution, although smaller $H\alpha$ emitting areas are also present. There is a tendency for $\text{HeI}7065/H\alpha$, $[\text{SII}]6717+6731/H\alpha$, and $[\text{SII}]+[\text{SIII}]/H\alpha$ to peak outside of the star-forming regions. The prominent ring-shaped structure in the $\text{HeI}/H\alpha$, $[\text{SII}]/H\alpha$, and $[\text{SII}]+[\text{SIII}]/H\alpha$ diagrams immediately to the right of the minor axis and centered on HA is discussed in the text.

the ‘outer arc’ originates near the left hand edge of Figure 5, and is resolved into sub-structures in Figure 2 of Otte & Dettmar (1999). While the outer arc is not obvious in the $H\alpha$ measurements, pockets of bright $\text{HeI}7065$ and $[\text{SII}]$ emission in Figure 5 coincide with this feature.

The $\text{HeI} 7065$ line is one of the strongest He emission lines in the red part of the spectrum, and the $\text{HeI}7065/H\alpha$ ratio gauges variations in ionization conditions. Significant variations in the $\text{HeI}7065/H\alpha$ ratio are seen in Figures 5 and 6. The $\text{HeI}7065/H\alpha$ ratio tends to be lowest in HII regions, and there is only modest nebula-to-nebula variation in this ratio. The one exception is HC, where $\text{HeI}7065/H\alpha$ is lower than in other star-forming regions, suggesting that ionization conditions in HC differ from those in the other nebulae.

The complex nature of the ISM in the central regions of NGC 55 is evident in the $[\text{SII}]/H\alpha$ ratios, and in Figure 5 it is clear that the strengths of $[\text{SII}]$ and $H\alpha$ are anti-correlated. This anti-correlation is a well known phenomenon in diffuse interstellar gas (DIG), and was first investigated in NGC 55 by Hoopes et al (1996). If the DIG is excited by photoionization from Lyman photons then the $[\text{SII}]/H\alpha$ ratio should increase with distance from the ionizing stars. Ferguson et al. (1996) find (1) a relation between $[\text{SII}]/H\alpha$ and $H\alpha$ surface brightness, in the sense of decreasing $[\text{SII}]/H\alpha$ with increasing $H\alpha$ surface brightness, and (2) that the $[\text{SII}]/H\alpha$ ratio in the main body of NGC 55 is $\sim 2\times$ higher than in individ-

ual HII regions. The $[\text{SII}]/H\alpha$ ratios obtained from the GMOS spectra show variations in excess of a factor of 2, with localized areas where the $[\text{SII}]/H\alpha$ ratio approaches $3\times$ that in HII regions.

A high $[\text{SII}]/H\alpha$ ratio is a signature of shocked gas, and $[\text{SII}]/H\alpha$ is commonly used to identify supernova remnants (SNRs). The $[\text{SII}]/H\alpha$ ratio in SNRs is typically ≥ 0.5 (e.g. Blair et al. 1981). The vast majority of SNRs in nearby galaxies have diameters in excess of 20 pc (e.g. Badenes et al. 2010; Long et al. 2010), and so would appear as extended sources in the GMOS spectra of NGC 55. Despite the high SFR, there are no areas in Figures 4 – 6 where the $[\text{SII}]/H\alpha$ threshold is breached, although we caution that the numbers shown in Figures 4 – 6 are made over angular scales that correspond to $\sim 60\times 60$ parsecs.

There is a large ring-like structure with a diameter of 200 – 300 parsecs that is immediately to the right of the minor axis in Figure 5 that has moderately high $[\text{SII}]/H\alpha$ ratios. This structure is also seen in the $\text{HeI}/H\alpha$ ratio, and is more-or-less symmetric about the $H\alpha$ source HA, the spectrum of which is examined in Section 4.2. We suggest that the emission from the ring is powered by an outflow from the HA star-forming region. The symmetric nature of the ring-like structure is perhaps surprising given its proximity to H4, as any outflow from the larger star-forming complex might be expected to compress the ring. Still, the orientation of NGC 55 is

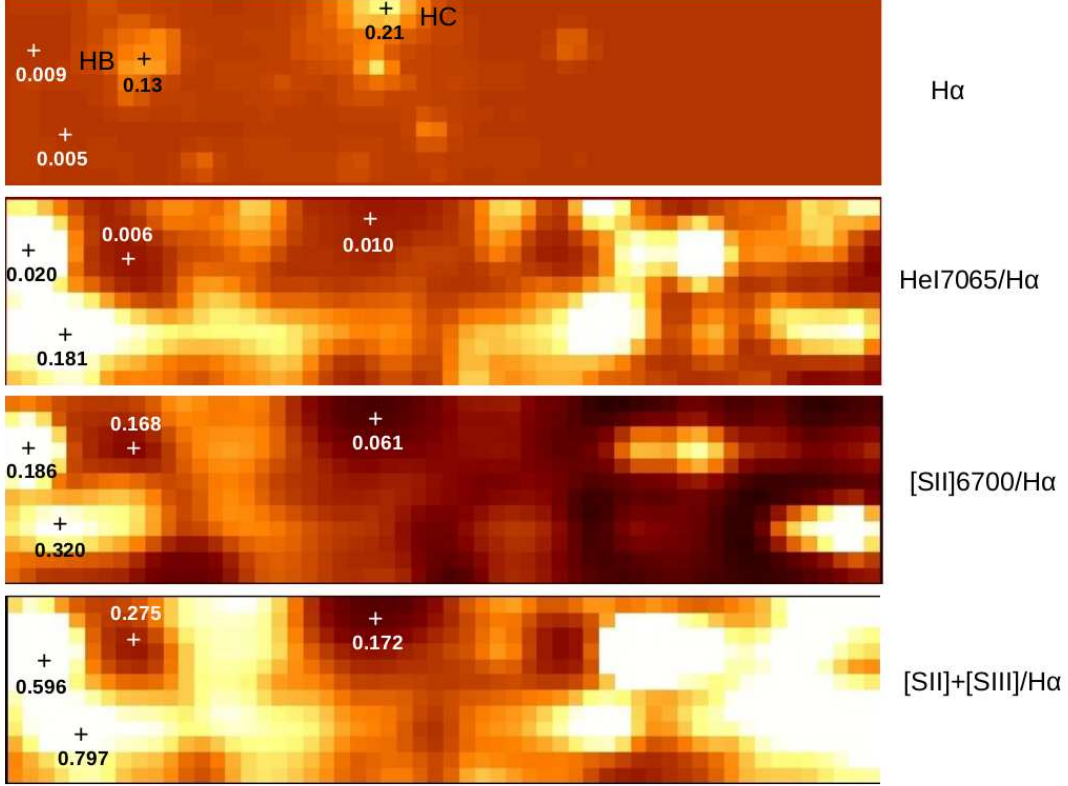


FIG. 6.— Same as Figure 4, but for the right hand third of the area observed with GMOS in Figure 1. Localized areas of star formation dominate the $H\alpha$ map, and HB and HC are star-forming regions that are discussed in the text. The surface brightness in this part of NGC 55 at visible/red wavelengths is lower on average than in the areas displayed in Figures 4 and 5. Line measurements that depart markedly from those that are more typical throughout the area observed with GMOS tend to occur where low signal levels affect line strength measurements.

such that the physical distance between the ring and H4 might be larger than the projected value.

The $[SIII]9069$ line is a prominent feature at wavelengths where the extinction from dust is lower than at visible/red wavelengths, although it is in a part of the spectrum that coincides with deep telluric water bands. The $[SIII] 9069$ line is significant from an astrophysical perspective since – when combined with the strengths of the $[SII]$ lines at 6717 and 6731 Å – it is an estimator of $[S/H]$. Vilchez & Esteban (1996) define the S_{23} statistic as the sum of the $[SII]$ doublet with the $[SIII]$ lines at 9069 and 9532 Å normalized to the strength of $H\beta$.

S_{23} can not be computed from the GMOS data as $H\beta$ was not observed. In lieu of S_{23} , the sum of $[SII]6700$ and $[SIII]9069$ divided by $H\alpha$ is shown in Figures 4 – 6. This ratio depends on metallicity and the ionization state, and so it is not surprising that it varies with location in the area observed with GMOS. The $[SII]+[SIII]/H\alpha$ ratios in HB, H4, H9, HA, and H2 are remarkably similar, arguing that these nebulae likely have similar $[S/H]$ and ionization conditions. An exception is HC, where $[SII]+[SIII]/H\alpha$ is one half that in the other nebulae, and it should be recalled that the $HeI7065/H\alpha$ ratio in HC is also distinct. Of the star-forming regions considered here, HC has the largest projected distance from the center of NGC 55, and so might be expected to have a slightly lower mean metallicity than star-forming regions with smaller projected distances from the galaxy

center. However, to the extent that the gas in the NGC 55 plane is well-mixed so that there are no major abundance variations, then the line ratios in HC more likely point to ionization conditions in that nebula that differ from those in the other star-forming regions.

4.2. The Spectra of Individual Star-Forming Regions

Spectra of the H2 and H4 star-forming complexes, constructed by averaging signal in areas where $H\alpha$ emission is at least one-half of the peak value detected with GMOS, are shown in Figure 7. These spectra thus sample areas with the highest concentration of young stars, and so provide estimates for when the most recent large-scale episode of star formation occurred in each complex. As NGC 55 is viewed almost edge-on, there is a contribution to the light from stars and gas that are not part of these star-forming regions. The contribution from such contaminating light was estimated from areas that are adjacent to each complex, and the mean spectrum constructed from these measurements was subtracted from the H2 and H4 spectra. As Figures 4 – 6 demonstrate, emission line ratios are not spatially uniform throughout this part of NGC 55, and this introduces obvious uncertainties when correcting for background light. However, the background signal tends to be modest when compared with the light from the much brighter star-forming complexes.

Emission lines in H2 have larger equivalent widths

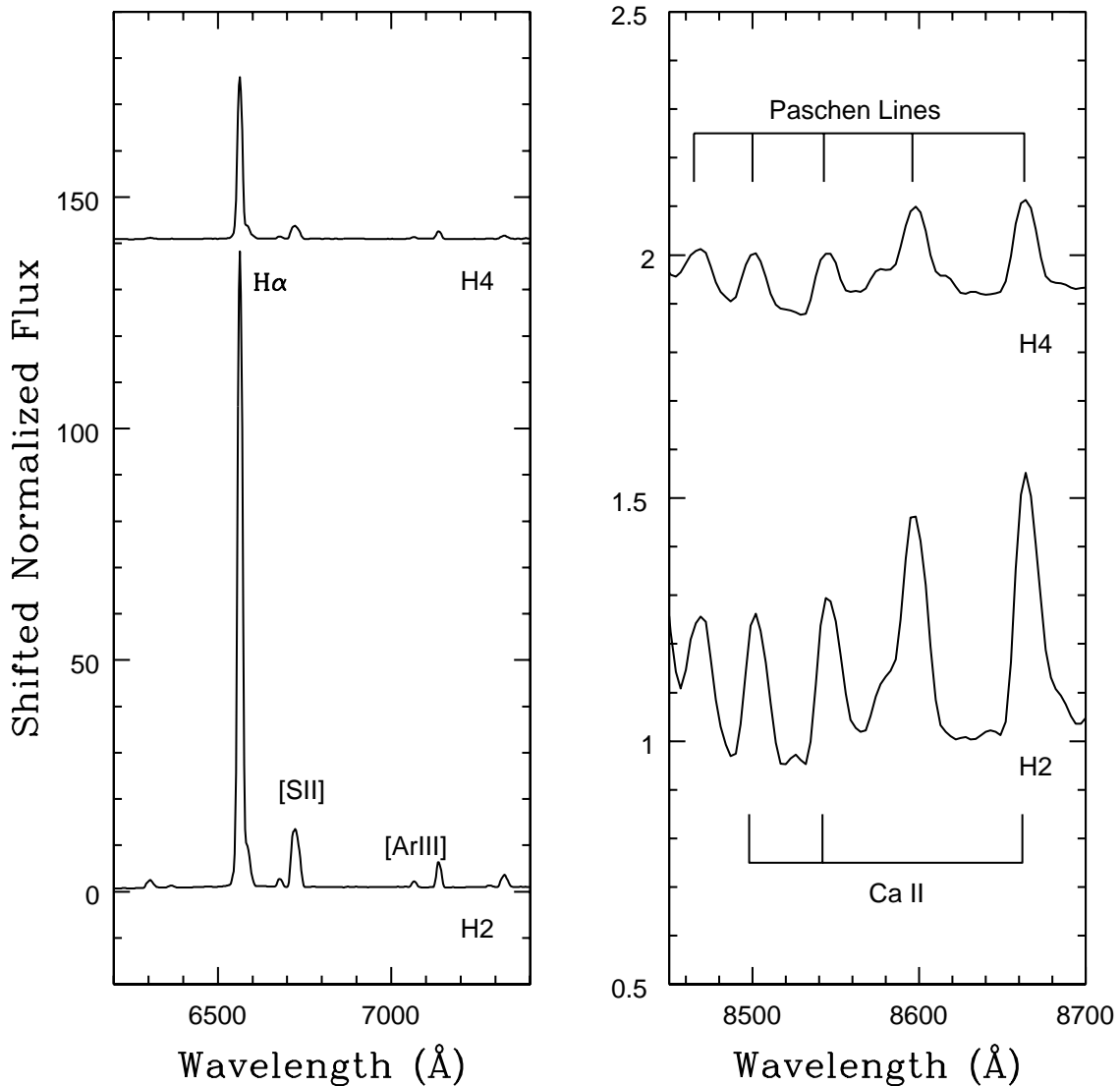


FIG. 7.— Spectra of H2 and H4, constructed by combining signal in areas where H α emission is at least one half of the peak value in the area observed with GMOS. Wavelengths near H α and the near-infrared Ca triplet are shown. The spectra have been normalized to the continuum, and corrected for background light by subtracting the mean spectra of adjacent areas. The H4 spectra have been shifted vertically for display purposes. Emission lines in H2 are more pronounced than in H4, suggesting that H2 contains hotter, more massive stars than H4. Wavelengths that sample Ca II lines are contaminated by Paschen series emission, complicating the detection of Ca absorption from luminous red stars.

than in H4. This is likely an age effect, with H2 containing hotter, more massive (and presumably younger) ionizing stars than in H4. The equivalent width of H α in H2 is $\sim 1700\text{\AA}$ while in H4 it is $\sim 560\text{\AA}$. This places H2 on the flat part of the relation between the equivalent width of H α and time since the onset of star formation shown in Figure 83 of Leitherer et al. (1999), with an age $\log(t_{yr}) \leq 6.4$, and a best estimate of $\log(t_{yr}) \sim 6.2$. In contrast, H4 is on the rapidly descending part of this relation, with an age $\log(t_{yr}) \sim 6.7$. Therefore, assuming that H2 and H4 are simple stellar systems that experienced an instantaneous burst of star formation and that each have $Z=0.008$, then the last major episode of star formation in H2 was within the past 2.5 Myr, whereas in H4 it was ~ 5 Myr in the past.

We caution that the age estimates made in the previous paragraph are based on spectra of the brightest

part of the nebulae, and so probe mainly the most recent large-scale episode of star formation. Sub-structuring in star-forming complexes might be expected as the location of star formation within a giant molecular cloud may shift with time. In fact, compact HII regions are found near the edge of H2 (Section 5), indicating that star formation is not centrally concentrated in that complex. Large star-forming complexes may thus contain stars that formed over timescales of a few tens of Myr (e.g. De Marchi et al. 2011; 2017), which is comparable to the disruption time scale of giant molecular clouds (e.g. Murray 2011). The young ages found for H2 and H4 based on the H α equivalent widths do not preclude on-going star formation in these complexes, as the emission line spectra of systems experiencing continuous star formation reach an equilibrium value of a few Myr after the onset of star formation (Byler et al. 2017).

RSGs appear $\sim 6 - 8$ Myr after the onset of star formation, and spectroscopic signatures from such stars would then provide constraints on the duration of star formation. The Ca triplet lines are the deepest absorption features at red wavelengths in the spectra of RSGs, and are prominent features in the spectra of simple stellar systems with ages between $\sim 6 - 25$ Myr (e.g. Figure 97 of Leitherer et al. 1999). Unfortunately, emission lines from the Paschen sequence dominate the part of the spectrum that contains the Ca triplet, which is shown in the right hand panel of Figure 7.

The challenges imposed by nebular emission aside, older stellar generations will likely develop a more diffuse spatial distribution than that of the youngest stars (e.g. De Marchi et al. 2017). Spectroscopic signatures of RSGs might then be seen in areas close to H2 and H4 where line emission is weaker. In Section 4.3 it is shown that there are areas adjacent to H4 where deep Ca triplet lines are seen.

The spectra of other prominent $H\alpha$ sources in Figures 5 and 6, which we name HA, HB, and HC are compared in Figure 8. HA is at the center of the ring-shaped structure in the [SII]/ $H\alpha$ and HeI/ $H\alpha$ distributions that is to the immediate right of the minor axis of NGC 55. The equivalent width of $H\alpha$ in HA is comparable to that in H4, and the Paschen emission lines at wavelengths near 8600\AA have amplitudes like those in H4, suggesting similarities among the stars that power photoionization.

HB and HC are prominent sources of $H\alpha$ emission in Figure 6, and the latter has a projected distance of ~ 1 kpc from the center of NGC 55. The FUV-NUV colors shown in Figure 2 indicate that HC is the furthest area of large-scale star formation from the center of NGC 55 in the north west portion of the disk. The equivalent width of $H\alpha$ in HB and HC is slightly larger than in HA and H4, but is weaker than in H2. The Paschen emission lines in HB are more pronounced than in HA and H4, and this could indicate that the ionization state of HB differs from that in HA or H4, possibly due to differences in the mix of stellar types that produce the ionizing radiation. [SII] is also stronger in HB than in either HA or HC, but [SII]/ $H\alpha$ in HB is smaller than in H2. The equivalent width of $H\alpha$ in HC is smaller than in H2, although the Paschen emission lines in HC and H2 have similar equivalent widths.

4.3. Absorption Features

The Ca triplet and the CN band head near 7900\AA are prominent absorption features in the spectra of evolved late-type stars. The spatial behaviour of the indices defined in Table 2 that measure the depths of these absorption features is examined in Figure 9. Low signal levels prevent the measurement of the Ca3 and CN7900 indices near the ends of the GMOS slit, and so only the area near the center of NGC 55 – covering the same spatial interval as in Figure 5 – is shown. As the CN7900 and Ca3 indices probe features in the spectra of cool stars, the corresponding portion of the SPITZER [3.6] image is also shown in Figure 9. The $H\alpha$ measurements from Figure 5 are also repeated there.

If the stars that dominate the near-infrared light are uniformly mixed throughout the central regions of NGC 55 then any changes in the projected distribution

of the CN7900 and Ca3 indices would be due to non-uniform veiling by continuum emission. Paschen emission lines also overlap with lines of the Ca triplet. If continuum and line emission played a significant role in defining the depths of absorption features then the depths of absorption features and the equivalent width of $H\alpha$ emission would be coupled.

The area shown in Figure 9 covers a range of $H\alpha$ equivalent widths, and there is a tendency for the areas of weakest Ca3 and CN7900 to occur where $H\alpha$ emission is strongest. Still, the areas of deepest Ca absorption are not exclusively found where the equivalent width of $H\alpha$ is smallest, but instead tend to occur between H4 and HA, near the minor axis of NGC 55. There are other areas with comparatively deep CN7900 and Ca triplet absorption in Figure 9, indicating that the stars that produce the deep absorption features are not restricted to the area near the minor axis, but are in what may be clusters or associations located throughout the area shown in Figure 9.

There is a concentration of luminous red stars in the [3.6] image in the lower panel of Figure 9 that coincides with the pocket of deep Ca triplet absorption between H4 and HA. The mean spectrum of the area marked in Figure 9 is shown in Figure 10. The wavelength interval near $H\alpha$ is shown in the left hand panel, while the wavelength interval that includes the Ca lines is shown in the right hand panel. Also shown is the median of the continuum-corrected spectra of the entire area sampled with GMOS. This spectrum notionally shows the ‘typical’ spectroscopic characteristics in this part of NGC 55.

The equivalent widths of $H\alpha$ emission in the two spectra in Figure 10 are comparable. The similarity in $H\alpha$ equivalent widths notwithstanding, the Ca triplet lines in the Center spectrum are deeper than in the median spectrum. The deep Ca absorption is attributed to the luminous red stars – which likely are RSGs – in the [3.6] image. The pockets of deep CN7900 absorption near the left hand edge of Figure 9 where CN7900 is very strong are not associated with obvious stellar groupings in the [3.6] image.

There is an absence of bright red stars in the [3.6] image in the main bodies of H4, H9, and HA, and this can be used to set an upper limit to the time since the onset of star formation in these locations. It is unlikely that luminous red stars are present but obscured by dust in these areas, as gas tends to be ejected from star clusters on timescales that are comparable to the onset of supernovae, which occur a few Myr after the start of star formation (e.g. Hollyhead et al. 2015). For comparison, the RSG phase of evolution starts $6 - 8$ Myr after the initiation of star formation, and so this evolutionary phase is expected to occur after gas is ejected. The absence of RSGs suggests that the areas of present-day large-scale star formation in Figure 9 have been forming stars for timescales of no more than a few Myr.

While H4, H9, and HA may be relatively young structures, the presence of RSGs throughout the central regions of NGC 55 indicates that large scale star formation has been on-going for at least many Myr. In fact, the spatial distribution of RSGs in the [3.6] image is clumpy, suggesting that there are numerous fossil star-forming regions near the center of NGC 55. A large population

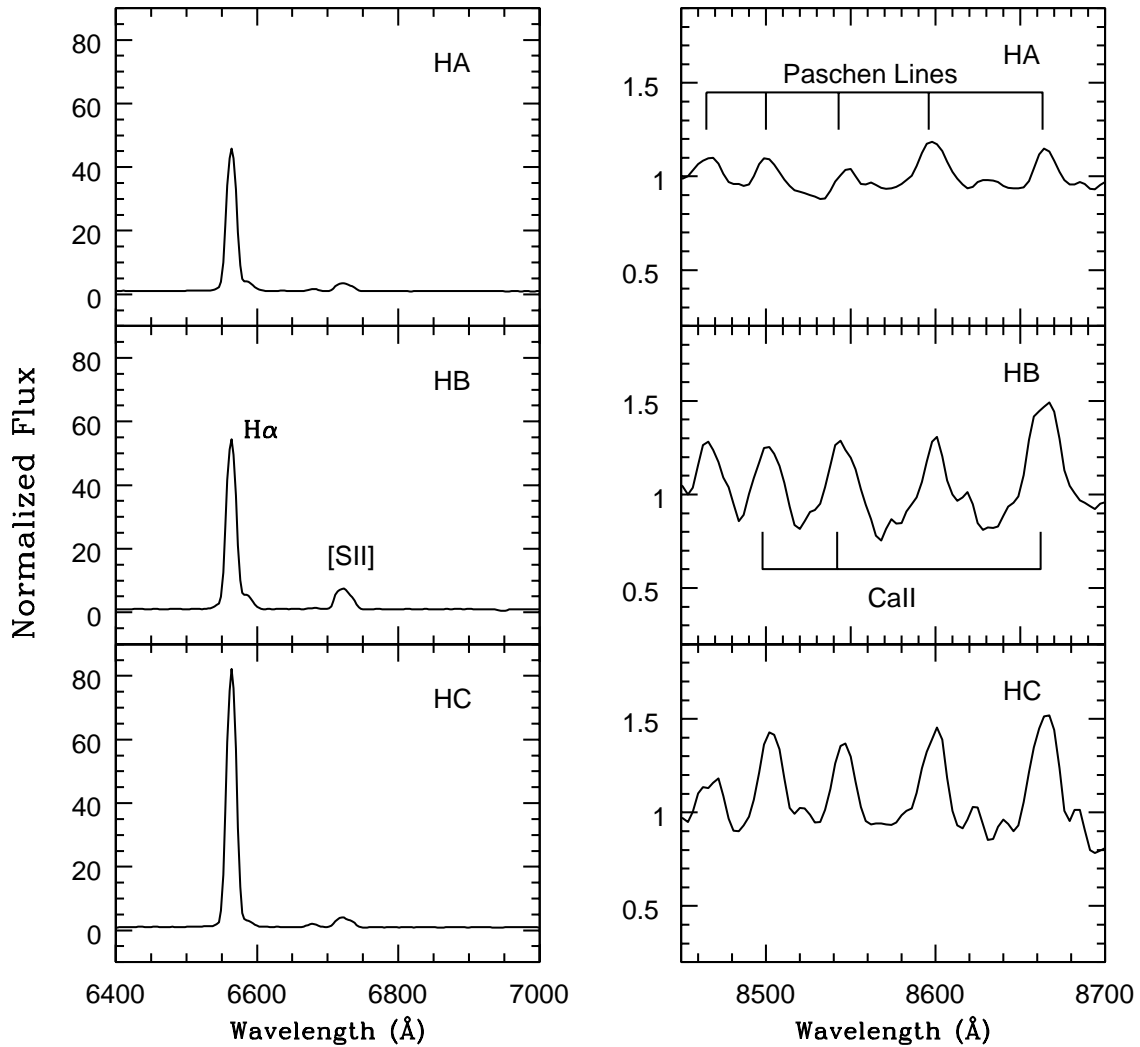


FIG. 8.— Same as Figure 7, but showing spectra of the HA, HB, and HC star-forming areas. Emission lines from the Paschen series dominate the wavelength interval that contains the near-infrared Ca triplet.

of luminous young red stars near the center of NGC 55 is not unexpected. Engelbracht et al. (2004) use MIPS images to examine the star-forming activity in NGC 55, and find that roughly one-third of the flux at $24\mu\text{m}$ originates from compact regions, almost all of which are near the center of the galaxy. They estimate a global star formation rate (SFR) for NGC 55 of $0.22 M_{\odot} \text{ year}^{-1}$, and the SFR in compact regions is then $\sim 0.07 M_{\odot} \text{ year}^{-1}$. If star formation in this part of NGC 55 proceeded at a constant rate for 10^7 years – which is the timescale consistent with the presence of RSGs – then $\sim 10^6$ solar masses of stars would have been produced assuming a solar neighborhood-like mass function. This corresponds to ~ 50 clusters similar in size to The Arches, which has a mass of $2 \times 10^4 M_{\odot}$ (Espinoza et al. 2009). A larger mass of stars would have formed if star formation proceeded continuously near the center of NGC 55 at this rate for more than 10^7 years.

5. POINT SOURCES

A number of bright point sources are present in the GMOS observations, and the spectroscopic properties of these are discussed in this section. It is unlikely that the objects found here are individual stars given the high stellar density near the center of NGC 55, coupled with the ~ 1.5 arcsec FWHM image quality of these data. Instead, many – if not all – are undoubtedly either asterisms, compact nebulae, and/or compact star clusters that appear as a bright single object (e.g. Figure 15 of Stephens et al. 2003).

Sources were identified by eye in individual disk spectra. This was done because the 2 arcsec wide slit makes the detection of individual objects with sizes of 1 - 1.5 arcsec FWHM in mosaiced images problematic – meaningful angular resolution measurements on sub-arcsec scales are only available in the direction along the spectrograph slit. Emphasis was also placed on relatively bright point sources so as to obtain spectra with moderately high S/N ratios, and so an automated detection algorithm was deemed to be unnecessary. Source identi-

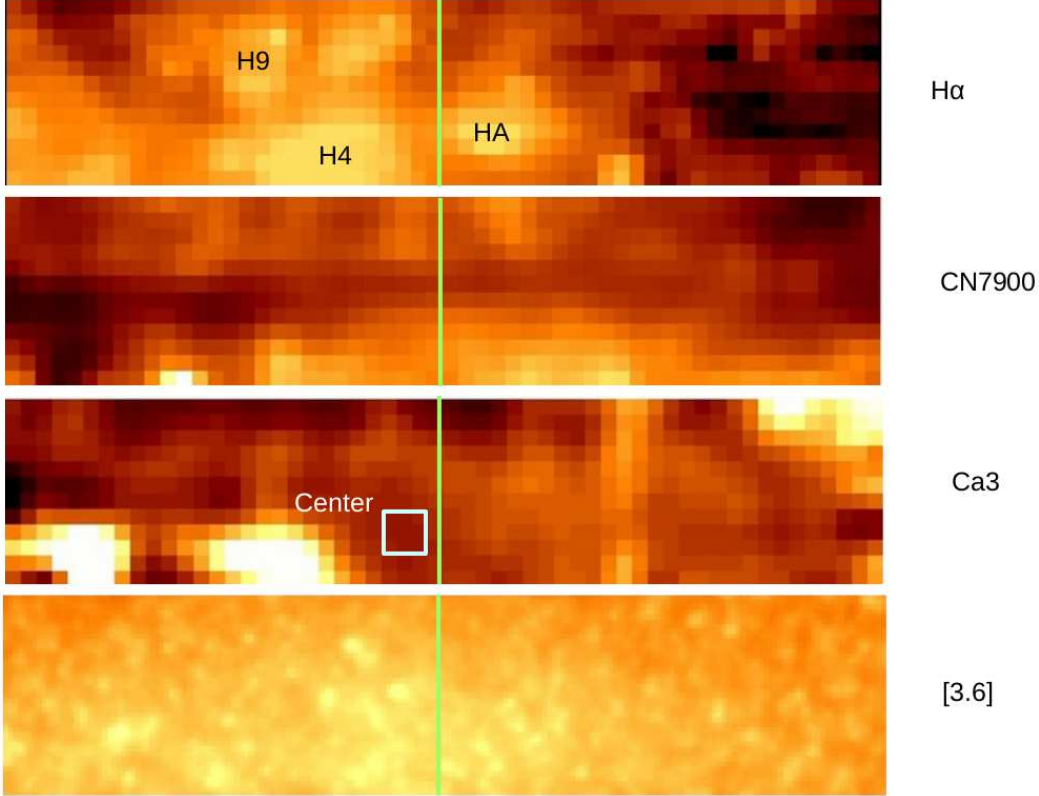


FIG. 9.— Distribution of $H\alpha$ (top panel), CN7900 (second panel) and Ca3 (third panel) indices in the spatial interval examined in Figure 5. The indices are displayed with a logarithmic stretch with darker shades corresponding to deeper features. The bottom panel shows this same area imaged in [3.6]. The minor axis of NGC 55 is indicated with a green line. The distribution of CN7900 and Ca3 indices shows structure that tends to be anticorrelated with $H\alpha$, in the sense that weak Ca3 absorption is found in areas with strong $H\alpha$ emission. Still, there are exceptions. An area with deep Ca3 absorption is seen to the right of H4 near the minor axis of NGC 55, and this corresponds to a concentration of luminous sources in the [3.6] image. Other areas with deeper than average Ca absorption are also seen above and to the left of H4. It is evident from the [3.6] image that the stellar content in this part of NGC 55 is not uniformly mixed, and that there is a population of luminous evolved stars close to the center of NGC 55. The blue square indicates the area where the Center spectrum plotted in Figure 10 was extracted.

fication was performed after collapsing the spectrum of each offset along the wavelength axis in the 7000 – 8500 Å interval to approximate the bandpass of the i' filter. The use of light over a wide wavelength range suppresses (but does not completely remove) a bias in favor of emission line objects. The success of removing this bias is borne out in the types of objects that are detected, as only some have prominent emission lines in their spectra.

Spectra of point sources were extracted by summing the signal within the FWHM of the seeing disk. Sources that are obvious blends were not considered unless the peak signal from the contaminating source was less than half that of the primary target, and was separated from that source by at least one FWHM. Spectra to monitor local background light were extracted in the area surrounding target objects, and the mean of these was subtracted from each extracted spectrum. Given the crowded nature of the central regions of NGC 55 and the non-uniform spatial distribution of ionization characteristics then there are cases in which a reliable local sky spectrum could not be obtained, and there is evidence of over- or under-subtraction of emission lines in some spectra.

Photometric measurements of these objects were

obtained from the [3.6] and [4.5] images discussed in Section 3. The angular resolution of the SPITZER images is not greatly different from that of the GMOS data, simplifying the task of matching targets in the two datasets. Photometry in these filters provides information about the nature of the sources, especially those in which the light is dominated by highly evolved cool stars.

The photometric measurements were made with the point spread function (PSF)-fitting routine ALLSTAR (Stetson & Harris 1988). A PSF for each filter was constructed from isolated bright stars, and routines in the DAOPHOT (Stetson 1987) package were used to obtain a source list and preliminary aperture photometry measurements. An object was considered to be detected only if it was identified in both the [3.6] and [4.5] images. The photometry was calibrated by applying the zeropoints measured by Reach et al. (2005). Only photometric measurements of point sources with spectra are discussed here; the photometry of a much larger sample of sources in and around NGC 55 detected in the SPITZER images will be presented in a separate paper (Davidge 2019, in preparation).

Sources were sorted by eye into six groups based on their spectroscopic properties: (1) HII regions, (2) early-type stars, (3) M giants/supergiants, (4) C stars,

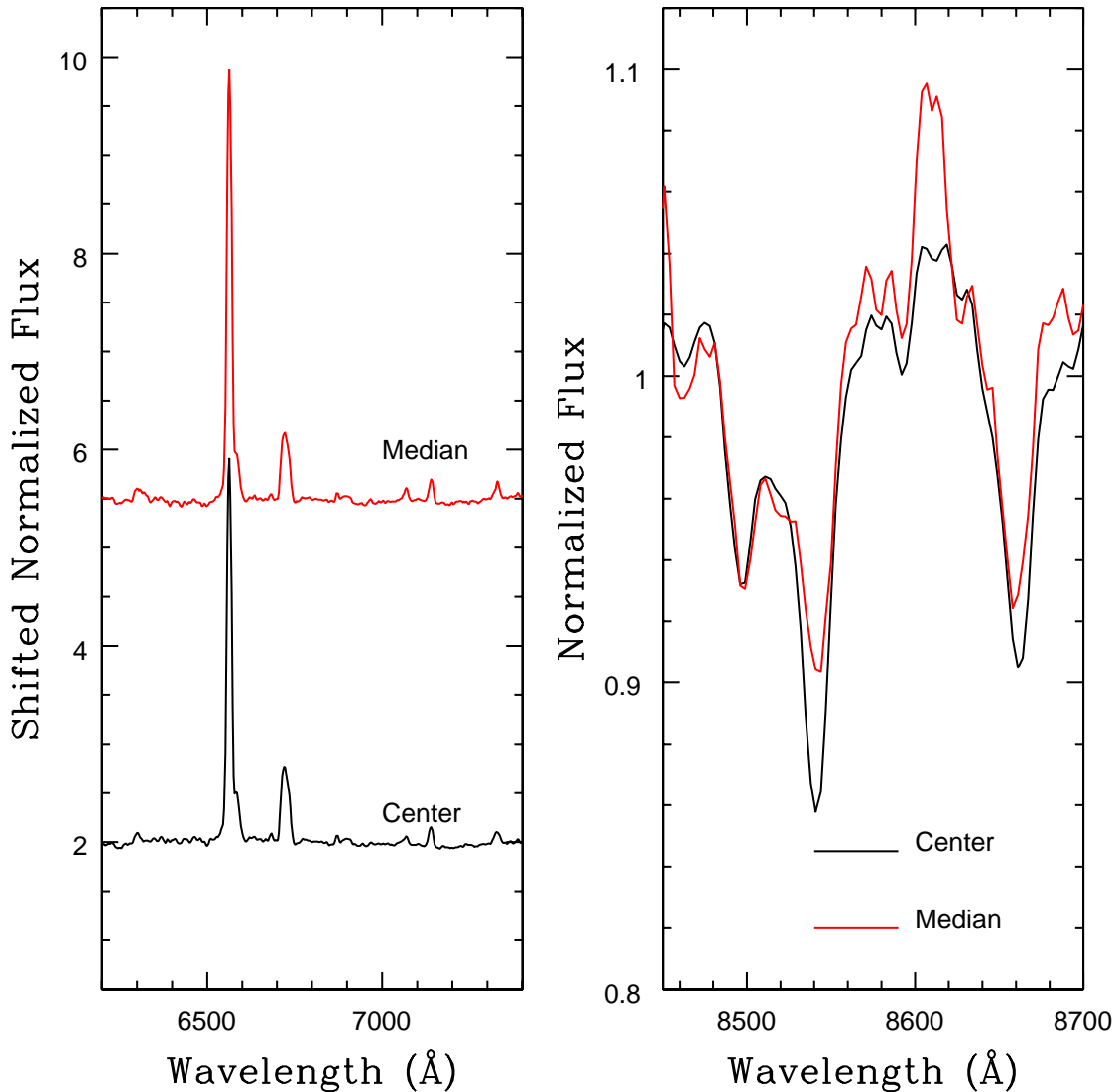


FIG. 10.— Mean spectrum of the area marked ‘Center’ in Figure 9, and the median spectrum of the entire area sampled with GMOS (‘Median’). The spectra have been normalized to the continuum, and those in the left hand panel have been shifted vertically for display purposes. $H\alpha$ emission in the Center spectrum is only slightly weaker than that in the Median spectrum. However, the Ca lines in the Center spectrum are much deeper than in the Median spectrum.

(5) composite systems that show a mix of spectroscopic signatures, and (6) objects with largely featureless spectra. Objects in the last two groups have no clear spectroscopic type and are not discussed further as they may be the result of unreliable sky subtraction. The locations of the objects in the first four groups are shown in Figure 11. The panels in this figure cover the same areas as those in Figures 4 – 6.

Magnitudes and locations of the sources are shown in Table 3. ΔX and ΔY refer to offsets in arcsec from the center of NGC 55, with the X axis paralleling the major axis of NGC 55. The sources are not distributed uniformly across the field, with the majority of objects that have star-like spectra located north of the major axis. This positional discrepancy is likely due to a number of factors. The line emission and amount of dust obscuration is greater in the southern half of the area observed than that has $\Delta X > 0$ than in the northern half of the field.

In addition, the image quality of some of the spectra in the southern half of the field is slightly poorer than in the northern half, although the difference is no more than a few tenths of an arcsec and is not expected to hinder greatly the detection of bright sources. In fact, most of the compact HII regions are found in the southern half of the GMOS field.

There is the potential for ambiguity when matching objects detected at widely different wavelengths given that the light might originate from very different mechanisms at each wavelength (e.g. photospheric light in the GMOS observations, versus the potential for significant levels of thermal emission in the SPITZER data). Differences in the levels of extinction between the wavelengths sampled by GMOS and SPITZER further complicate source matching, as do differences in angular sampling. The observations for this program were defined using images from the Digital Sky Survey (DSS), and the

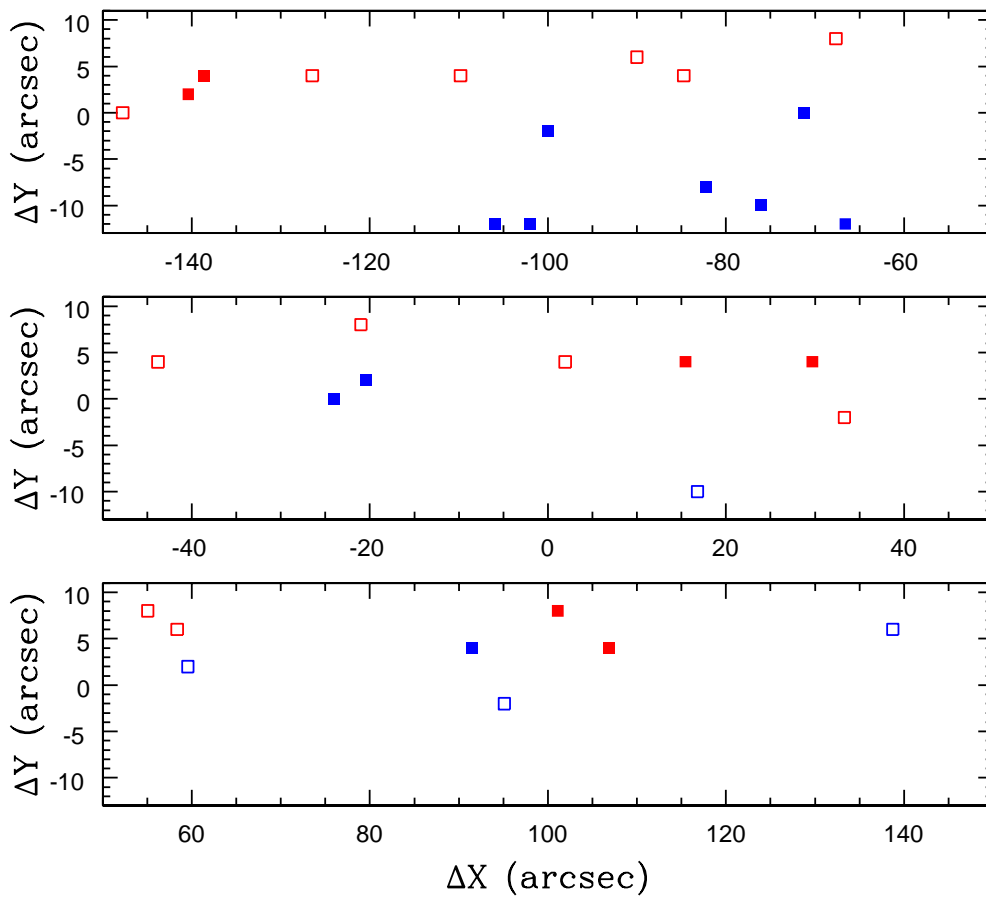


FIG. 11.— Locations of individual sources, with co-ordinates measured along the major and minor axes. The intersection of the major and minor axes define the origin of the co-ordinate system. The panels cover the same areas as in Figures 4 – 6, and the co-ordinates are listed in the second and third columns of Table 3. Sources with spectra classified as M-type (open red squares), C star-type (filled red squares), early-type (open blue squares), and HII region-like (filled blue squares) are shown. The majority of compact HII regions are located near H2 and H4, suggesting that they may be the result of star formation propagating throughout these areas. The remaining sources are distributed more-or-less uniformly over the northern part of the area observed with GMOS. This is an area where line emission is less intense and obscuration due to dust is lower than in the southern half of the area studied. The image quality in some of the spectra that sample the southern half of the field is also slightly poorer than in the northern half, although the difference in image quality is small enough so as not to markedly affect the detection of point sources.

DSS images were used to align the GMOS and SPITZER observations. Reference sources that were common to both datasets were identified. The alignment of the two datasets involved correcting for angle of rotation and differences in pixel sampling, followed by the application of offsets along the X and Y axes.

A GMOS source was considered to be matched to a SPITZER counterpart if the co-ordinates agreed to within 3 arcsec. While 3 arcsec is a generous matching radius, it is only $1.5\times$ the FWHM of the SPITZER [3.6] observations and the width of the GMOS slit. Past experience indicates that a matching criterion of $1 - 2\times$ FWHM is sufficient to identify real source matches, while limiting the numbers of false matches. In any event, the majority of matched sources have co-ordinates that agree to much better than 3 arcsec. The co-ordinates of sources that did not have photometric detections, and so are based solely on GMOS-derived co-ordinates, are

shown in brackets.

The $([4.5],[3.6]-[4.5])$ CMD of the spectroscopically-identified point sources is shown in Figure 12. Many of the objects scatter about $[3.6]-[4.5] \sim 0$, which is the locus of sources that have effective temperatures higher than a few thousand K. There is also a population of bright objects that have comparatively red $[3.6]-[4.5]$ colors, and these are sources where thermal emission from hot dust likely contributes to the SED. The majority of sources are at least 1 magnitude above the faint limit of the SPITZER observations, which is indicated by the dashed line in Figure 12. This is not unexpected as the comparatively shallow GMOS observations will detect only relatively bright sources.

5.1. Compact HII Regions

The spectra of sources with emission lines that might be indicative of HII regions are shown in Figure 13.

TABLE 3
SOURCES WITH ANGULAR SIZES COMPABLE TO THE SEEING DISK

ID	Type	ΔX (arcsec)	ΔY (arcsec)	RA (2000)	Dec (2000)	[4.5]	[3.6]–[4.5]
p4-4	HII	(74.4)	(3.6)	(00:14:46.8)	(–39:11:23.2)	–	–
p2-7	HII	–37.8	4.2	00:14:58.1	–39:12:10.3	14.16	0.39
c-5	HII	–40.2	–1.8	00:14:58.2	–39:12:18.7	16.14	–0.40
c-6	HII	(–88.2)	(–0.6)	(00:15:03.1)	(–39:12:36.8)	–	–
m2-5	HII	–114.6	0.0	00:15:05.7	–39:12:48.2	15.13	0.70
m8-3	HII	(–99.6)	(–9.0)	(00:15:03.9)	(–39:12:51.6)	–	–
m10-5	HII	–91.8	–9.6	00:15:03.1	–39:12:49.7	16.18	–0.12
m12-1	HII	–82.8	–13.2	00:15:02.0	–39:12:50.3	16.30	–0.50
m12-2	HII	(–119.4)	(–12.6)	(00:15:05.8)	(–39:13:04.4)	–	–
m12-3	HII	(–123)	(–12.0)	(00:15:06.1)	(–39:13:05.6)	–	–
p8-2	M	34.8	5.4	00:14:50.8	–39:11:37.8	14.87	0.26
p8-5	M	(–84.6)	(7.8)	(00:15:03.1)	(–39:12:27.6)	–	–
p6-6	M	(–107.4)	(6.0)	(00:15:05.1)	(–39:12:39.7)	–	–
p4-9	M	–13.8	2.4	00:14:55.6	–39:12:02.0	15.47	0.60
c-10	M	–165.6	–2.4	00:15:10.8	–39:13:11.9	16.61	–0.25
m2-3	M	17.4	–1.2	00:14:52.4	–39:11:53.1	15.69	0.17
p8-3	M	–37.8	7.2	00:14:58.0	–39:12:04.1	16.63	–0.09
p6-3	M	39.0	6.6	00:14:50.5	–39:11:33.8	16.98	–0.11
p4-10	M	–60.0	3.6	00:15:00.4	–39:12:20.5	15.11	0.27
p4-13	M	–100.2	4.8	00:15:04.4	–39:12:36.3	16.30	0.01
p4-14	M	–123.6	4.2	00:15:06.8	–39:12:47.1	16.49	0.18
p4-15	M	–140.4	3.6	00:15:08.4	–39:12:57.8	16.04	–0.03
p8-1	C	85.2	10.2	00:14:45.9	–39:11:10.8	15.28	0.60
p4-1	C	90.0	3.0	00:14:45.2	–39:11:17.9	14.92	0.58
p4-5	C	11.4	2.4	00:14:53.1	–39:11:50.8	14.73	0.45
p4-7	C	(–1.8)	(3.6)	(00:14:54.5)	(–39:11:55.7)	–	–
p4-16	C	–154.8	6.6	00:15:10.2	–39:12:54.0	16.57	0.36
p2-12	C	(–157.2)	(1.8)	(00:15:10.1)	(–39:13:04.3)	–	–
p6-1	OB	178.2	5.4	00:14:36.4	–39:10:36.5	16.57	–0.06
p2-4	OB	(84.6)	(1.2)	(00:14:45.7)	(–39:11:20.8)	–	–
m2-2	OB	126.0	177	00:14:41.4	–39:11:08.5	15.91	–0.47
m10-4	OB	32.4	166	00:14:51.0	–39:11:41.8	15.91	0.11

As the sources discussed in this section were selected because they are compact, then the spectra of larger, more extended areas of $H\alpha$ emission in Figures 4 – 6 are not included in this figure. With one exception, the compact HII regions are found near the outer boundaries of H2 and H4, and this spatial distribution suggests that these are pockets of localized star formation that are triggered by activity within the larger star-forming complexes.

The emission and absorption features in the Figure 13 spectra may be affected by the non-uniform distribution of line emission in the areas used to estimate background light levels. Keeping this caveat in mind, the typical ratio of $[SII]/H\alpha$ in Figure 13 is comparable to that in H2 and H4, as expected if the emission is due to photoionization that originates close to the ionizing stars. The $[SII]/H\alpha$ ratio also indicates that none of the objects are compact SNRs.

Paschen line emission is seen in the spectrum of cen–6, which also has the strongest $H\alpha$ emission line. However, Ca triplet absorption lines are also seen in some of the HII spectra, suggesting that luminous red stars – presumably RSGs – contribute significantly to the light. This absorption is most obvious in the spectra of n2-5 and cen–5. There is comparatively weak $H\alpha$ emission in the spectra of those sources, and so veiling from continuum emission and contamination from Pa emission lines is likely to be less of a factor than in sources with stronger $H\alpha$ emission. Still, the spectrum of p2-7 indicates that weak $H\alpha$ emission is not a guarantee that the Ca triplet

will be detected. There thus appears to be source-to-source variations in the red stellar content that is the source of the Ca triplet lines.

What is the nature of the sources that produce Ca absorption in Figure 13? It is unlikely that the Ca lines originate from a widely dispersed, uniformly distributed population, as the signatures of such a population would be suppressed during background subtraction. Still, the spatial resolution of the GMOS data at the distance of NGC 55 is $\sim 20 \times 20$ parsecs, and so the stars that are the source of the Ca lines may not physically coincide with the HII region. Luminous red stars might be expected near large star-forming complexes if there has been star-forming activity for an extended period of time. If star formation has been on-going in n2-5 and cen–5 for at least 6 – 8 Myr then the Ca absorption may originate from an older population that has had time to diffuse away from the present-day star-forming region. If these stars are free from areas of high extinction then the contrast between the Ca triplet lines and Pa line emission will be much more favorable for the detection of stellar absorption lines. Alternatively, RSGs and luminous AGB stars could originate in older clusters that have ages in excess of ~ 8 Myr and are located close to the HII regions.

Half of the HII regions were matched with sources in the SPITZER observations, and those that were matched have a broad range of [3.6]–[4.5] colors. The light from the objects detected by SPITZER likely orig-

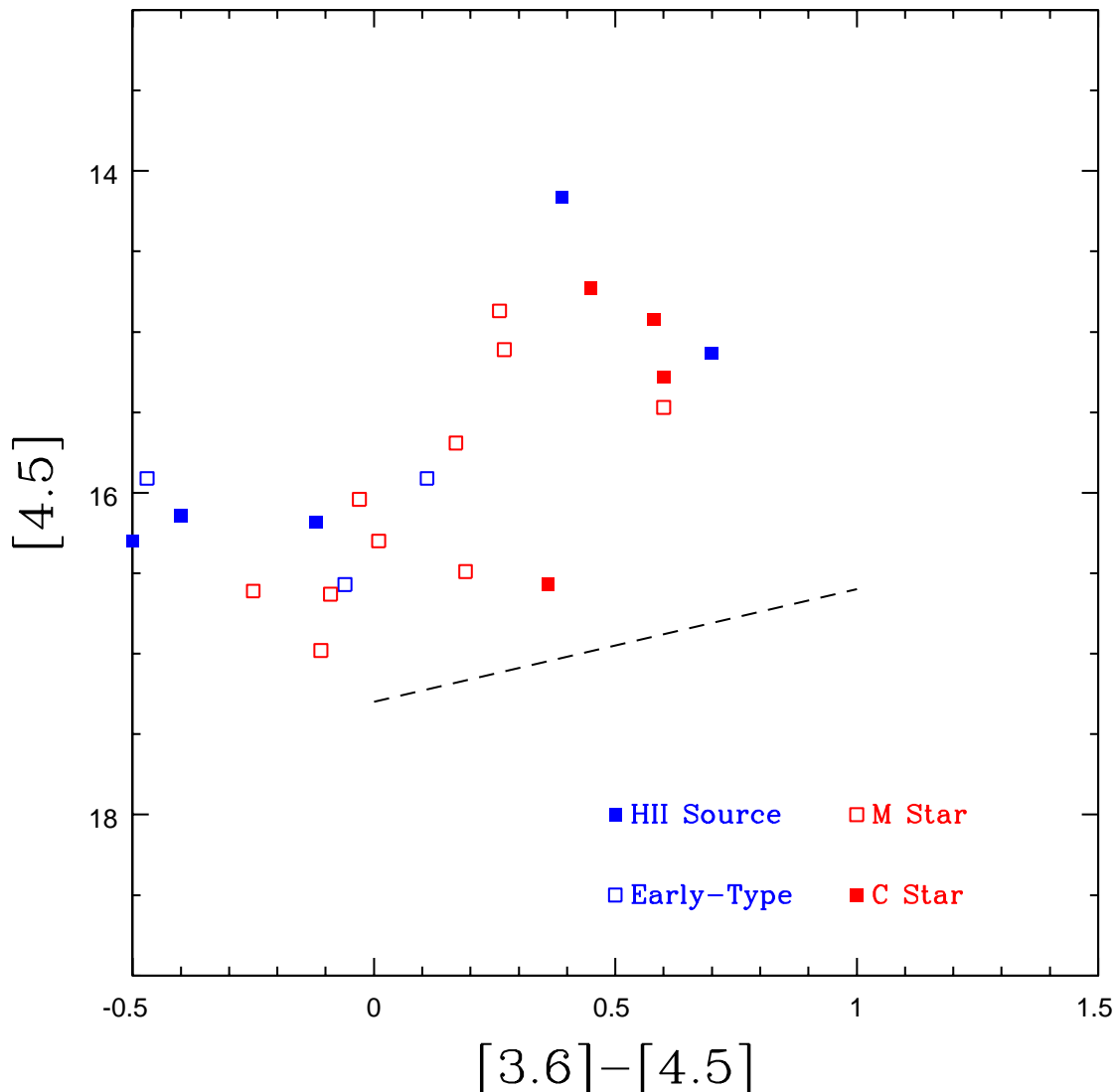


FIG. 12.— The $([4.5], [3.6] - [4.5])$ CMD of point sources in the GMOS spectra. The light from each of these objects likely comes from many stars, although a small number of objects may dominate the light output at these wavelengths. The dashed line shows the faint limit of the SPITZER observations. Objects in which the light originates from sources with effective temperatures in excess of a few thousand K have $[3.6] - [4.5] \sim 0$. The broad color distribution of sources that are matched with HII regions reflects the diverse SEDs of sources within star-forming areas. The two bright, red sources associated with HII regions are probably highly obscured young clusters.

inates from stars/star clusters within the HII region. These are expected to have a diverse range of SEDs that reflect differences in the amount of obscuration and the effective temperatures of the embedded sources. The brightest spectroscopically-identified point source in $[4.5]$ is associated with an HII region, and this is probably a highly obscured young cluster located inside the HII region. There is no correlation between $[3.6] - [4.5]$ color and the detection of Ca triplet lines in the spectrum.

5.2. Early and Late-Type Spectra

Spectra of objects with characteristics that are indicative of early-type stars are shown in Figure 14. The spectra of these sources have prominent Paschen series absorption lines, and the Paschen break near $0.82\mu\text{m}$ is seen in all four spectra. Whereas the Paschen line characteristics of the four spectra in Figure 14 show good source-to-source agreement, this is not the case for $\text{H}\alpha$.

While $\text{H}\alpha$ is in absorption in three spectra, it appears that the $\text{H}\alpha$ and $[\text{SII}]$ emission lines in the spectrum of m10-4 have been over-subtracted. This illustrates the difficulty obtaining reliable $\text{H}\alpha$ strengths in areas with non-uniform line emission.

The light from the objects with spectra in Figure 14 is likely dominated by a single bright blue supergiant (BSG) or a small number of BSGs. The dominant source of light is/are then objects that have ages of no more than a few tens of Myr. Three of the four objects with early-type spectroscopic characteristics were matched with SPITZER sources, and the $[3.6] - [4.5]$ colors of these suggest that thermal emission does not contribute significantly to the infrared light. If red stars are present within 10 – 20 parsecs of the BSGs – as might be expected if the BSGs are in clusters or associations – then those red stars do not have large-scale circumstellar

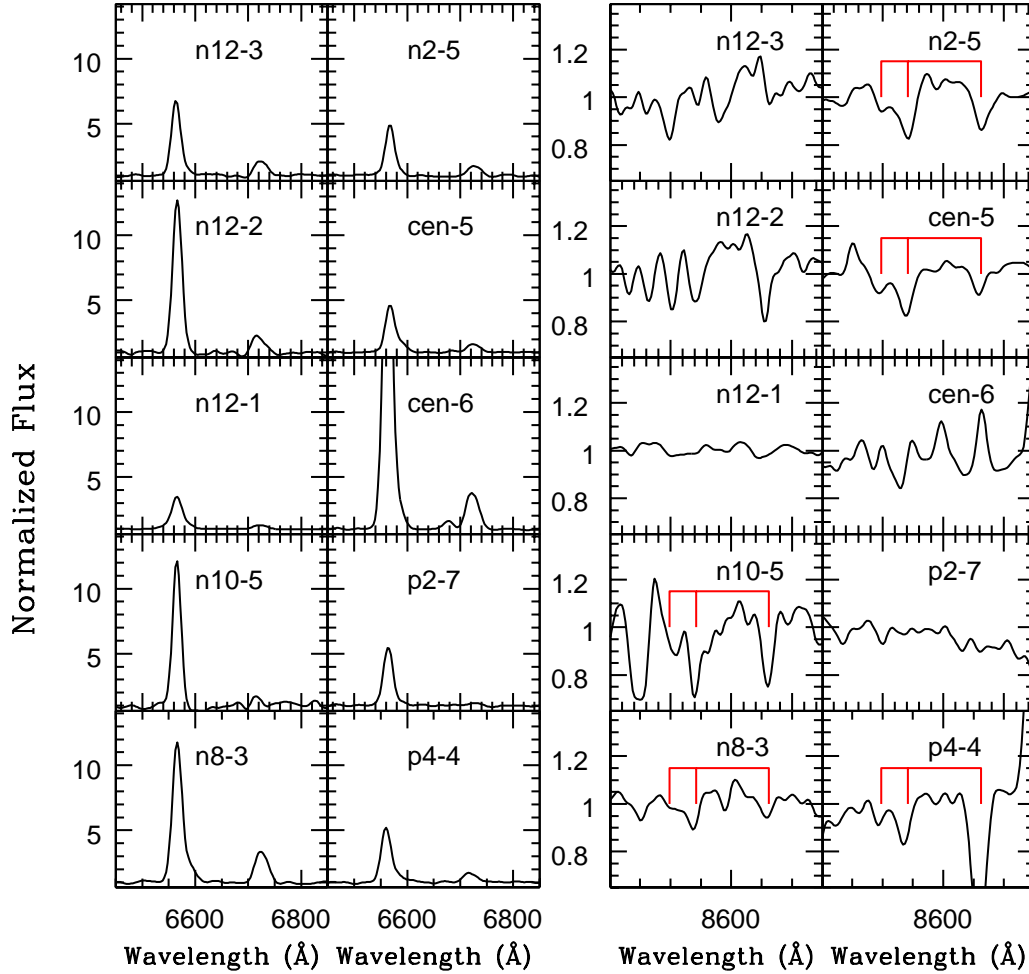


FIG. 13.— Spectra of compact sources classified as HII regions. Wavelengths near $H\alpha$ are examined in the left hand panel, while wavelengths centered on the near-infrared Ca triplet are covered in the right hand panel. The spectra have been normalized to the continuum. All objects have $[SII]/H\alpha$ ratios that are consistent with photoionization generated close to the ionizing source(s); none are SNRs. $H\alpha$ emission is strongest in cen-6, and in many cases the emission lines in the Pa series are clearly seen in the wavelength interval containing the Ca triplet. Still, some of the spectra have prominent Ca triplet absorption, indicating that luminous red stars are concentrated within ~ 10 parsecs of the line-emitting regions. The wavelengths of the Ca triplet lines are marked in those spectra. The abnormally strong Ca line near 8662\AA in the p4-4 spectrum is likely due to poor sky subtraction caused by non-uniformities in the background light.

envelopes, such as those that are found around the most luminous AGB stars.

Sources with early-type spectroscopic characteristics are restricted to $X > 15$ arcsec in Figure 11, suggesting that they do not have an obvious physical connection with the present-day activity in H2 and H4. Still, we caution that the distribution of point sources is likely affected by selection effects, as the detection of stars/compact clusters in the part of the GMOS observations with negative offsets in X and Y is complicated by line emission. BSGs in or near star-forming regions might also evade detection if they are obscured by dust along the line of sight.

Spectra of sources with TiO bands longward of $0.71\mu\text{m}$ are shown in Figure 15. The Ca triplet is also

seen in the spectra of all twelve objects, and it is likely that the objects with spectra in this figure are star clusters where the red/near-infrared light is dominated by M supergiants. If this is correct then these sources have ages $\sim 10 - 100$ Myr.

The majority of the sources with spectra in Figure 15 were detected in both [3.6] and [4.5], and these have a broad range of [3.6]–[4.5] colors. This is consistent with the MIR SEDs of Galactic M giants, which also span a range of [3.6]–[4.5] colors (e.g. Reiter et al. 2015). While sources with late-type spectroscopic features are found in the northern half of the area observed with GMOS, as with BSGs this distribution might be due to selection effects.

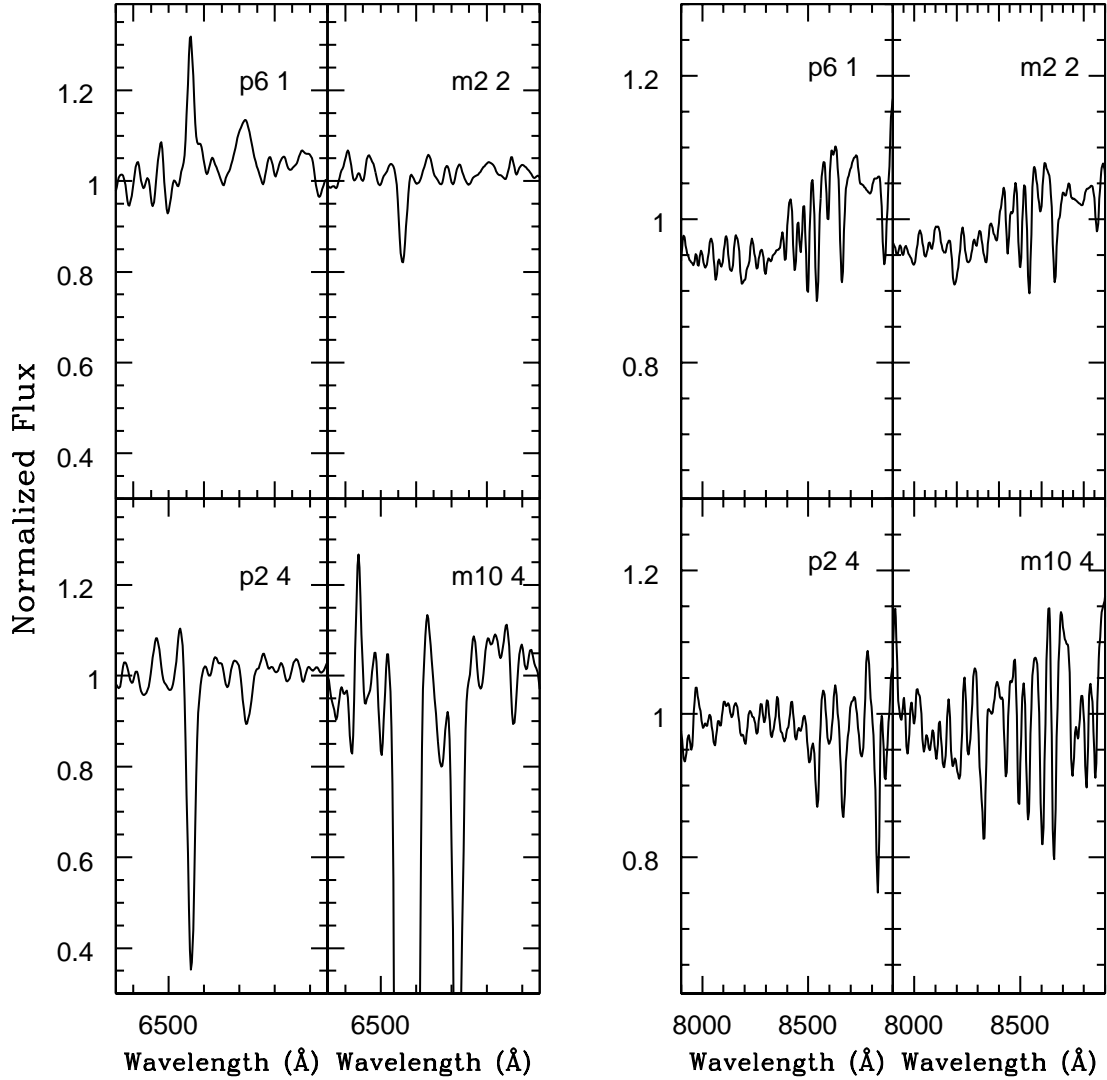


FIG. 14.— Spectra of sources where the light is dominated by early-type stars. The spectra have been normalized to the continuum. Prominent Paschen line absorption is detected in all four sources, and the Paschen break is seen near 8200 Å. With the exception of p6-1, these objects have H α in absorption. However, the spectra in the left hand panel illustrate how uncertainties in background subtraction can affect H α characteristics, as the extremely deep H α and [SII] lines in the spectrum of m10-4 are likely due to the over-subtraction of nebular emission lines. The depths of the H α absorption lines may also be affected by H α emission that is intrinsic to the sources.

5.3. Sources with Broad CN bands

C stars have been detected in significant numbers in the outer regions of NGC 55 (Pritchett et al. 1987), and are likely also present in the central regions of the galaxy. Individual C stars can be detected in the outer regions of NGC 55 as the stellar density is low, so that there is minimal dilution of the CN bands by contaminating light. While crowding makes the detection of single stars challenging in dense environments like the central regions of NGC 55, luminous C stars produce distinct signatures in the integrated spectra of at least some intermediate age LMC clusters (Davidge 2018a), opening the possibility that these features might be detected even if the light from a C star is blended with that of other objects. Luminous AGB stars are also photometrically variable, and they may dominate the signal from a resolution element when near the peak of their light curves

(Davidge et al. 2010).

Figure 16 shows the GMOS spectra of six unresolved sources that have broad CN bands. Four of these were detected in the Spitzer images, and these have [3.6]–[4.5] colors that are consistent with them being highly evolved, intrinsically luminous objects that have the circumstellar dust envelope that is found around many C stars. Also shown in Figure 16 are two spectra from Davidge (2018a): one is the spectrum of 2MASS05284449–6614309, which is the brightest C star in the LMC cluster NGC 1978, while the other is the spectrum of NGC 1978 Pointing 3 (P3). The latter is included to demonstrate how the integrated light from a cluster is affected by the presence of a C star. NGC 1978 has an age of 1.9 Gyr (Mucciarelli et al. 2007), which is similar to the luminosity-weighted mean age estimated for NGC 55 at red/NIR wavelengths by Davidge

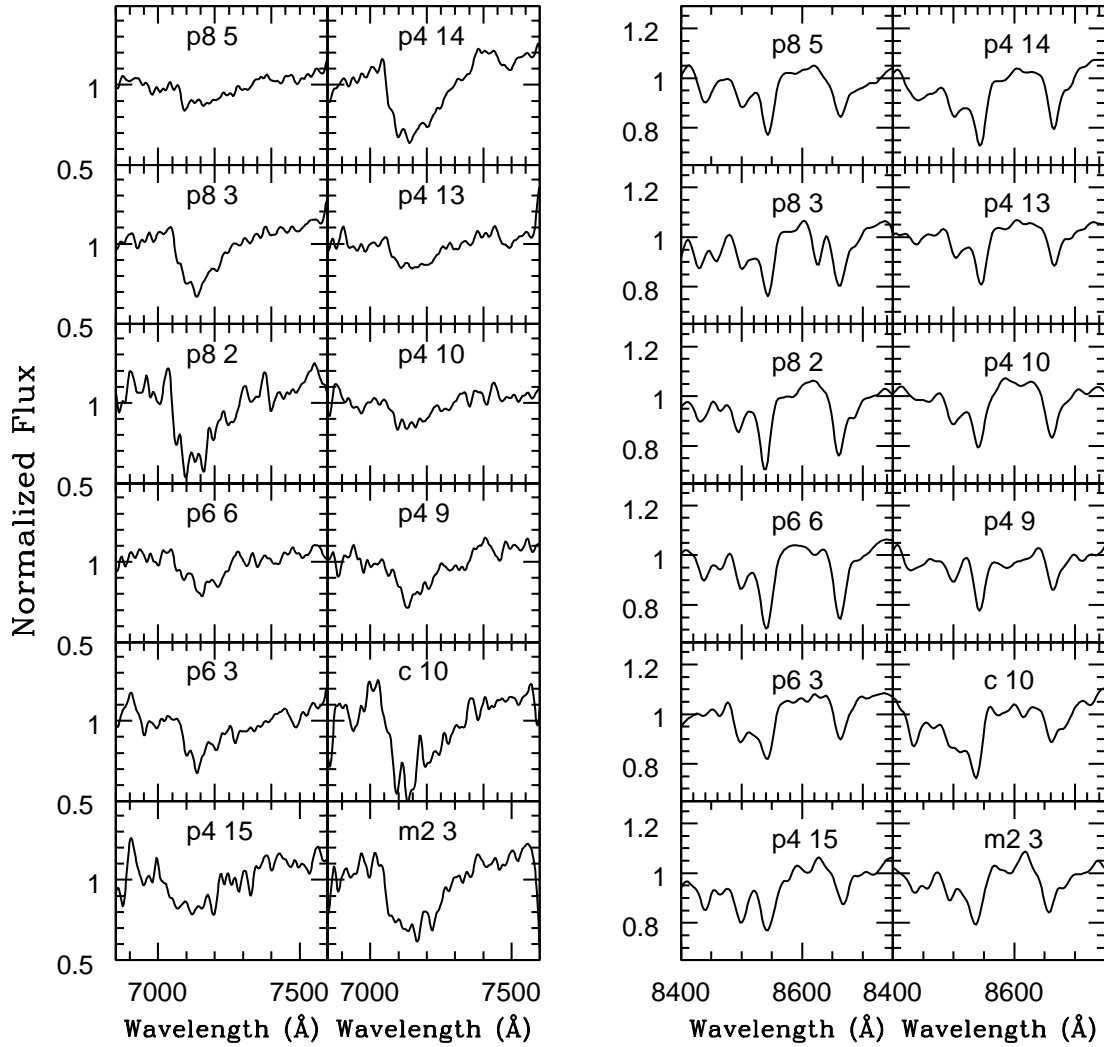


FIG. 15.— Spectra of point sources that have deep TiO bandheads at 7100\AA , indicating that the light is dominated by M giants. The spectra have been normalized to the continuum. Absorption lines of the Ca triplet are also present. The light from these sources is likely dominated by one or more RSGs.

(2018a).

The spectra of NGC 55 sources in Figure 16 have CN bands between 0.7 and $0.9\mu\text{m}$ that are similar in shape and depth to those in NGC 1978 P3, and we suspect that these objects are compact intermediate age clusters with ages similar to that of NGC 1978. The spatial distribution of these objects is also consistent with them being AGB stars. Davidge (1998) found that luminous AGB stars in the southern half of NGC 55 are well-mixed over kpc spatial scales. The six NGC 55 sources in Figure 16 are distributed across the field sampled by GMOS, as expected for objects that have ages that allow them to disperse over large distances from their birth environments.

There is a remarkable similarity between the spectra of the NGC 55 sources in Figure 16 and NGC 1978 P3, and we suspect that this is largely a selection effect. The noise level in the GMOS spectra is such that clusters in which the C star contributes a much smaller

fraction of the total signal than that from NGC 1978 will likely not have detectable CN bands. As for systems that might have stronger CN bands, it is anticipated that these will be rare in a crowded environment if observed with a ~ 20 parsec intrinsic resolution, as it would require a large number of C stars in one cluster or the fluke detection of an extremely luminous C star in a low mass cluster. The probability of either occurrence is low given the rapid pace of C star evolution.

6. DISCUSSION & SUMMARY

Long-slit spectra recorded with GMOS on GS that sample red and near-infrared wavelengths have been used to examine the projected distribution of emission and absorption features throughout the central regions of the nearby dwarf galaxy NGC 55. The results can be summarized as follows:

1) The central regions of many late-type galaxies show evidence for on-going or recent star formation, and NGC

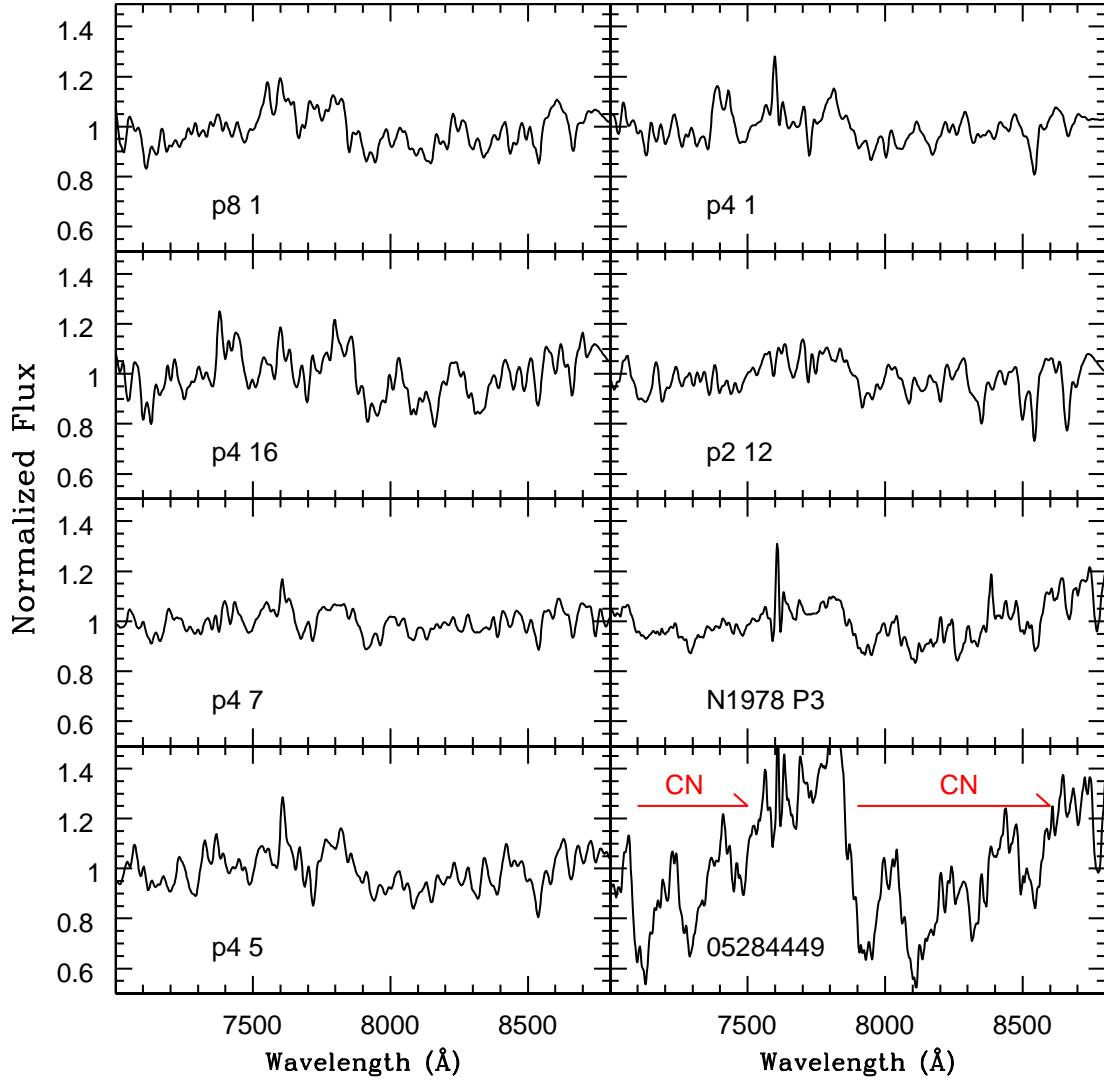


FIG. 16.— Spectra normalized to the continuum of sources with CN absorption bands. Two spectra from Davidge (2018a) are also shown: (1) the spectrum of the C star 2MASS05284449–6614309, which is the most luminous C star in NGC 1978, and (2) the spectrum of LMC cluster NGC 1978 Pointing 3 (P3), which shows the light of 2MASS05284449–6614309 combined with that of the underlying cluster. A comparison of the spectra of NGC 1978 P3 and 2MASS05284449–6614309 indicates that while the CN bands that are signatures of C stars are subdued in integrated light, they can still be detected in the composite spectrum. The depths of the CN bands in the NGC 55 sources suggest that the light originates from a stellar system, rather than a single star. The similarity between the spectra of the sources in NGC 55 and NGC 1978 P3 is likely a selection effect (see text).

55 is no exception. Much of the light from the H2 and H4 star-forming complexes at red wavelengths originates from line and continuum emission, with no evidence of Ca triplet absorption. The absence of Ca triplet absorption is consistent with the non-detection of luminous red stars in [3.6] images, suggesting that star formation in H2 and H4 has continued for only a few Myr. The spectra of three other large star-forming regions (HA, HB, and HC) have also been investigated. The equivalent widths of H α in these areas are comparable to those in H2 and H4, indicating that large star-forming areas in the disk of NGC 55 extend out to projected distances of ~ 1 kpc from the galaxy center.

2) Evidence is found for fossil star-forming regions near the center of NGC 55. Davidge (2005) discussed *J* and *K* observations of the center regions of NGC 55. Areas near

H4, identified as ‘Cluster 1’ by Davidge (2005), and H2, identified as ‘Cluster 2’, contain a population of bright resolved RSGs, with ages ~ 10 Myr. A concentration of bright stars or star clusters are also seen near H4 and HA in the Spitzer [3.6] images in the lower panel of Figure 9. Similar concentrations of red stars are not obvious near HB and HC. The presence of bright red stars suggests that recent star formation within a few hundred kpc from the center of NGC 55 has been on-going for at least many Myr.

There is a concentration of bright red sources in the [3.6] image near the intersection of the major and minor axes of NGC 55. These stars are distributed over ~ 200 parsecs, which is the approximate upper limit for the size of a GMC (Murray 2011). This central fossil star-forming region is part of an area with elevated light

levels in the [3.6] luminosity profile in the lower panel of Figure 1. There is also localized deep Ca absorption in the integrated spectrum that is attributed to these stars. Even if many of these sources are blends or clusters, a concentration of very red compact clusters would also be a signature of recent large-scale star formation.

Westmeier et al. (2013) find non-circular motions near the center of NGC 55 that they interpret as the signature of material that is channeled into the central regions by a bar. The centrally-concentrated population of luminous red stars and the evidence of on-going star formation in this area may then be the results of such a gas inflow. If the inflow of gas continues then it may affect the appearance of the center of the galaxy by assembling a moderately massive stellar nucleus or even bulge, assuming that the mass function is like that in the solar neighborhood.

That fossil star-forming regions are found near the center of NGC 55 is perhaps not surprising given that the current SFR in the central regions of NGC 55 is $0.07 M_{\odot} \text{year}^{-1}$ (Section 4). This is similar to the SFR in the Central Molecular Zone (CMZ) of the Galaxy during at least the past few Myr (e.g. Barnes et al. 2017). The recent SFR in the CMZ has been sufficient to produce large clusters like The Arches and The Quintuplet. Similar rich stellar concentrations might then be expected near the center of NGC 55, and candidate structures are seen in the [3.6] image in Figure 9.

3) In addition to examining integrated light throughout the center of NGC 55, the spectra of objects that are point sources at angular resolutions of ~ 1.5 arcsec FWHM have also been examined. While a single bright object (or a handful of objects) might dominate the light from such sources, these “point” sources are almost certainly composite stellar systems. Some are compact HII regions, and these are potentially important as they may provide constraints on abundance gradients when compared with abundances measured from HII regions at larger radii. There is debate as to whether or not there is a metallicity gradient in the NGC 55 disk, and most of the metallicity tracers considered to date are outside of the crowded central regions of the galaxy (e.g. discussion by Magrini et al. 2017 and Patrick et al. 2017). While there is uncertainty as to the physical location of objects within the galaxy, the majority of the compact HII regions found in the present study are in the peripheral regions of H2 and H4, suggesting a physical connection with these structures.

4) The spectra of some compact HII regions contain absorption lines of the NIR Ca triplet. This suggests that the areas in and/or around these HII regions harbor concentrations of luminous red stars when compared with the surrounding areas. The resolution elements that contain these HII regions thus contain stars with ages that span at least ~ 10 Myr.

5) The spectra of some unresolved objects suggest that their red/NIR light is dominated by early-type stars, while the spectra of others suggest that the light is dominated by RSGs or bright AGB stars. If these objects are star clusters then they will appear as diffuse structures in images with an angular resolution of ~ 0.1 arcsec.

6) A subset of point sources have spectra that show CN absorption bands, suggesting that C stars make a large contribution to the light at red wavelengths. Clusters

that contain very bright C stars are of interest for probing the star formation history (SFH) of NGC 55 during intermediate epochs (e.g. Maraston 2005). The depths of the CN bands are similar to those in the spectra of the LMC cluster NGC 1978, which has an age of 1.9 Gyr (Mucciarelli et al. 2007). While this similarity is likely a selection effect (Section 5), the discovery of clusters in NGC 55 with spectroscopic properties like NGC 1978 may not be unexpected given the various lines of evidence that support large scale star formation in NGC 55 a few Gyr in the past (e.g. discussion by Davidge 2018a, and below).

We close by discussing the evolution of NGC 55. The outer isophotes of NGC 55 have a lenticular shape, hinting that it is structurally distinct from other nearby late-type disk galaxies (Davidge 2018b). Kudritzki et al. (2016) discuss the chemical evolution of NGC 55 and conclude that there is the large-scale accretion and outflow of material. If a large outflow persists then NGC 55 may eventually shed its ISM, leaving a gas-poor intermediate mass disk galaxy. Barway et al. (2013) compare the stellar contents of intrinsically bright and faint S0 galaxies, and find that whereas brighter S0 galaxies are dominated by older populations, lower mass lenticular systems contain a significant young component. Evidence for recent star formation is seen in nearby low mass S0 galaxies. NGC 404 and NGC 5102 are nearby moderate mass, S0 galaxies that have relatively old disks (Williams et al. 2010; Davidge 2015). However, both have nuclei that contain young or intermediate age stars (Seth et al. 2010; Davidge 2015). There is also evidence for previous episodes of star formation near their centers (e.g. Kacharov et al. 2018; discussion by Seth et al. 2010), indicating that their central regions are not simple stellar systems. Some low mass S0 galaxies in the Virgo cluster also host centrally-concentrated star formation (Davidge 2018c).

Barway et al. (2013) suggest that intrinsically bright S0s formed early-on, whereas fainter S0s are the result of secular processes. If disk galaxies are transformed into lenticular galaxies throughout the age of the Universe then transition objects should be seen today. That NGC 404 and NGC 5102 are located within a few Mpc suggests that transition objects may not be rare. In fact, based on the lenticular shape of its outer isophotes, coupled with a star-forming history that suggests that there was a major episode of star formation ~ 2 Gyr in the past, we suggest that NGC 55 is such a transition galaxy.

Could the physical cause of the proposed on-going morphological transformation be an interaction with another galaxy? A tidal interaction could explain the asymmetric distribution of stars and gas in the NGC 55 disk. The space velocities of NGC 300 and NGC 55 suggest that they may have interacted 1 – 2 Gyr in the past (Westmeier et al. 2013), and there is evidence for elevated levels of star formation in NGC 55 during intermediate epochs. Davidge (2018a) reviewed the SFH of NGC 55, and noted that the C star frequency is an order of magnitude higher than in the LMC and SMC (Battinelli & Demers 2005). Given that the mean metallicity of NGC 55 is comparable to that in the LMC then this argues that a larger fraction of the stellar mass of NGC 55 formed during intermediate epochs than in the

LMC. This is noteworthy as there are large peaks in the SFR of the LMC during the epochs in which the progenitors of C stars form (e.g. Rubele et al. 2012), and these have been attributed to interactions with the SMC and the Galaxy (e.g. Bekki & Chiba 2005). Rubele et al. (2012) estimate that 15 – 30% of the stellar mass in the parts of the LMC they studied formed at this time. The specific SFR of NGC 55 during intermediate epochs would then have been even larger than that in the LMC. There is a need to produce a detailed SFH of NGC 55 to place further constraints on the amplitude and duration of star-forming episodes in NGC 55 during the time of the proposed interaction.

Bekki & Chiba (2005) point out that globular clusters would likely have been produced during the violent star-forming episode in the LMC that was driven by interactions. If NGC 55 experienced a similar event then large compact star clusters may also have formed. While there are no known globular clusters associated with NGC 55, the proposed compact clusters that are thought to host the C stars found in the present study may be the consequence of large scale star formation during intermediate epochs.

The notion that NGC 55 experienced a major interaction during intermediate epochs is not without problems. While NGC 300 is an obvious candidate for the perturbing system, the star-forming history of NGC 300 is similar to that of NGC 2403 (Kang et al. 2017), suggesting that if an interaction with NGC 55 did occur it did not have a major impact on the stellar content of NGC 300. This is surprising as the tilted ring model applied to NGC 55 by Westmeier et al. (2013) yields a rotation curve that is similar to that of NGC 300, indicating comparable masses – naively, both galaxies would then

be expected to show signatures of an interaction if there was an encounter between them. Still, the C star frequencies of NGC 55 and NGC 300 are comparable (Battinelli & Demers 2005), suggesting similar SFRs during intermediate epochs.

Another problem with NGC 300 as the perturbing system is the comparatively low metallicity of the extraplanar HII regions examined by Tullmann et al. (2003), which indicate that NGC 55 is accreting (or has accreted) gas from a source other than the disk of a moderately large spiral galaxy like NGC 300. This being said, Westmeier et al. (2013) suggest ESO294–010 as a possible system that could have interacted with NGC 55. An interaction may also have involved a now defunct gas-rich dwarf galaxy. If the orbit of such a companion was coplanar with the disk of NGC 55 then it might be the cause of the asymmetric nature of the NGC 55 disk.

External interactions may not be required to form a lenticular galaxy. Intermediate mass disk galaxies that evolve in isolation are subject to multiple episodes of bar formation and buckling, ultimately resulting in the formation of pseudo-bulges (e.g. Kwak et al. 2017). If this occurred in NGC 55 then the buckling of the bar would have presumably spurred a large episode of star formation during intermediate epochs and produced isophotes with a lenticular shape. However, such a purely secular process does not explain the asymmetric distribution of the NGC 55 disk. Westmeier et al. (2013) suggest that ram pressure stripping may explain the asymmetric disk of NGC 55, although it is not clear how this could produce an extended tail of stellar material along the disk plane.

Thanks are extended to the anonymous referee for providing a prompt and helpful report.

REFERENCES

- Bacon, R., Accordo, M., Adjali, L., et al. 2010, *Proc. SPIEE*, 7735, 8
- Badenes, C., Maoz, D., Draine, B. T. 2010, *MNRAS*, 407, 1301
- Barnes, A. T., Longmore, S. N., Battersby, C., Bally, J., Kruijssen, J. M. D., Henshaw, J. D., & Walker, D. L. 2017, *MNRAS*, 469, 2263
- Barway, S., Waddekar, Y., Vaghmare, K., Kembhavi, A. K. 2013, *MNRAS*, 432, 430
- Battinelli, P., & Demers, S. 2005, *A&A*, 434, 657
- Bekki, K., & Chiba, M. 2005, *MNRAS*, 356, 680
- Blair, W. P., Kirshner, R. P., & Chevalier, R. A. 1981, *ApJ*, 247, 879
- Byler, N., Dalcanton, J. J., Conroy, C., & Johnson, B. D. 2017, *ApJ*, 840, 44
- Carlos Reyes, R. E., Reyes Navarro, F. A., Melendez, J., Steiner, J., & Elizalde, F. 2015, *Rev Mex AA*, 51, 135
- Castro, N., Urbaneja, M. A., Herrero, A., et al. 2012, *A&A*, 542, A79
- Davidge, T. J. 1998, *ApJ*, 497, 650
- Davidge, T. J. 2005, *ApJ*, 622, 279
- Davidge, T. J. 2015, *ApJ*, 799, 97
- Davidge, T. J. 2018a, *ApJ*, 856, 129
- Davidge, T. J. 2018b, *RNAAS*, 2, A206
- Davidge, T. J. 2018c, *AJ*, 156, 233
- Davidge, T. J., Beck, T. L., & McGregor, P. J. 2010, *PASP*, 112, 241
- De Marchi, G., Paresce, F., Panagia, N., et al. 2011, *ApJ*, 739, 27
- De Marchi, G., Panagia, N., & Beccari, G. 2017, *ApJ*, 846, 110
- de Vaucouleurs, J., de Vaucouleurs, A., Corwin, H. G., Buta, R. J., Pataler, G., & Fouque, P. 1991, *The Third Reference Catalogue of Galaxies*, Springer-Verlag: New York
- Engelbracht, C. W., Gordon, K. D., Bendo, G. J., et al. 2004, *ApJS*, 154, 248
- Espinoza, P., Selman, F. J., & Melnick, J. 2009, *A&A*, 501, 563
- Ferguson, A. M. N., Wyse, R. F. G., & Gallagher, J. S. 1996, *AJ*, 112, 2567
- Gil de Paz, A., Boissier, S., Madore, B. F., et al. 2007, *ApJS*, 173, 185
- Graham, J. A. 1982, *ApJ*, 252, 474
- Graham, J. A., & Lawrie, D. G. 1982, *ApJ*, 253, L73
- Hollyhead, K., Bastian, N., Adamo, A., Silva-Villa, E., Dale, J., Royon, J. E., & Gazak, Z. 2015, *MNRAS*, 449, 1106
- Hook, I. M., Jorgensen, I., Allington-Smith, J. R., Davies, R. L., Metcalfe, N., Murowinski, R. G., & Crampton, D. 2004, *PASP*, 116, 425
- Hoopes, C. G., Walterbos, R. A. M., & Greenawalt, B. E. 1996, *AJ*, 112, 1429
- Jarrett, T. H., Chester, T., Cutri, R., Schneider, S. E., & Huchra, J. P. 2003, *AJ*, 125, 525
- Kacharov, N., Neumayer, N., Seth, A. C., Cappellari, M., McDermid, R., Walcher, C. J., & Torsten, B. 2018, *MNRAS*, 480, 1973
- Kang, X., Zhang, F., & Chang, R. 2017, *MNRAS*, 469, 1636
- Karachentsev, I. D., Grebel, E. K., Sharina, M. E., et al. 2003, *A&A*, 404, 93
- Kudritzki, R. P., Castro, N., and Urbaneja, M. A. et al. 2016, *ApJ*, 829, 70
- Leitherer, C., Schaerer, D., Goldader, J., et al. 1999, *ApJS*, 123, 3
- Long, K. S., Blair, W. P., Winkler, P. F. et al. 2010, *ApJS*, 187, 405
- Magrini, L., Goncalves, D. R., & Vajgel, B. 2017, *MNRAS*, 464, 739
- Maraston, C. 2005, *MNRAS*, 362, 799

- Martin, D. C., Fanson, J., Schiminovich, D., et al. 2005, *ApJ*, 619, L1
- Mucciarelli, A., Ferraro, F. R., Origlia, L., & Fusi Pecci, F. 2007, *AJ*, 133, 2053
- Murray, N. 2011, *ApJ*, 729, 133
- Otte, B., & Dettmar, R.-J. 1999, *A&A*, 343, 705
- Pagel, B. E. J., Edmunds, H. G., Fosbury, R. A. E., & Webster, B. L. 1978, *MNRAS*, 184, 569
- Patrick, L. R., Evans, C. J., Davies, B., et al. 2017, *MNRAS*, 468, 492
- Pritchett, C. J., Richer, H. B., Schade, D., Crabtree, D., & Yee, H. K. C. 1987, *ApJ*, 323, 79
- Reach, W. T., Megeath, S. T., Cohen, M. et al. 2005, *PASP*, 117, 978
- Reiter, M., Marengo, M., Hora, J. L., & Fazio, G. G. 2015, *MNRAS*, 447, 3909
- Roth, M. M., Sandin, C., Kamann, S., et al. 2018, *A&A*, 618, A3
- Rubele, S., Kerber, L., Girardi, L., et al. 2012, *A&A*, 537, A106
- Seth, A. C., Cappellari, M., Neumayer, N., et al. 2010, *ApJ*, 714, 713
- Sheth, K., Regan, M., Hinz, J. L., et al. 2010, *PASP*, 122, 1397
- Skrutskie, M. F., Cutri, R. M., Stiening, R. et al. 2006, *AJ*, 131, 1163
- Stephens, A. W., Frogel, J. A., DePoy, D. L., et al. 2003, *AJ*, 125, 2473
- Stetson, P. B. 1987, *PASP*, 99, 191
- Stetson, P. B., & Harris, W. E. 1988, *AJ*, 96, 909
- Sturch, L., & Madore, B. 2012, *BAAS*, 2194, 1107
- Tikhonov, N. A., Galazutdinova, O. A., & Drozdovsky, I. O. 2005, *A&A*, 431, 127
- Toribio San Cipriano, L., Dominguez-Guzman, G., Esteban, C., et al. 2017, *MNRAS*, 467, 3759
- Tullmann, R., Rosa, M. R., Elwert, T., et al. 2003, *A&A*, 412, 69
- Vilchez, J. M., & Esteban, C. 1996, *MNRAS*, 280, 720
- Webster, B. L., & Smith, M. G. 1983, *MNRAS*, 204, 743
- Werner, M., Roellig, T., Low, F., et al. 2004, *ApJS*, 154, 1
- Westmeier, T., Koribalski, B. S., & Braun, R. 2013, *MNRAS*, 434, 3511
- Williams, B. F., Dalcanton, J. J., Gilbert, K. M., et al. 2010, *ApJ*, 716, 71